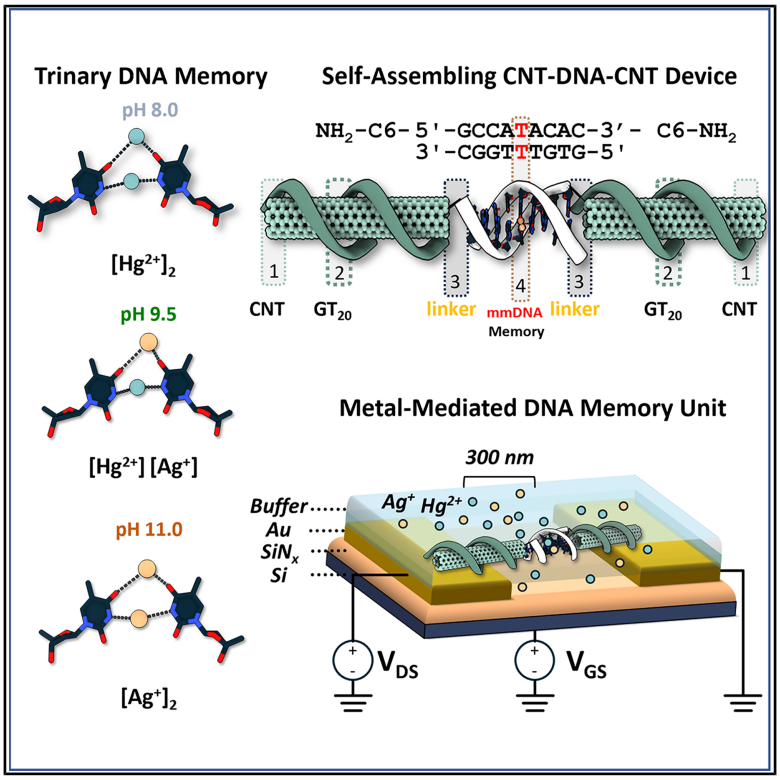
Matter

Article

Electrical control of a metal-mediated DNA memory

Graphical abstract



Highlights

- Single-molecule DNA memory: writable, readable, erasable on nanofabricated platform
- Precise, pH-mediated placement of metallic ions (Hg^{2+}, Ag^{+}) within the mmDNA
- DNA crystallography visualized the metal ion exchange, confirming the memory mechanism
- DNA memory switches 48 times, repeatedly readable with robust, rewritable function

Authors

Bo Liu, Brandon Lu, Arpan De, ..., M. P. Anantram, Simon Vecchioni, Joshua Hihath

Correspondence

anant@uw.edu (M.P.A.), sv1091@nyu.edu (S.V.), jhihath@asu.edu (J.H.)

In brief

As silicon-based memory nears its physical limits, DNA offers immense storage density but has lacked electronic integration. This work presents a fully electronic memory device from a single DNA molecule. Instead of using the genetic sequence, information is stored by electrically swapping individual metal ions at the DNA's core, switching the molecule between distinct, readable states. This direct electrical control of a molecule's atomic structure creates a rewritable memory, paving the way for molecular-scale systems compatible with modern electronics.

Development
Practical, real world, technological considerations and constraints

Liu et al., 2026, Matter 9, 102470
January 7, 2026 © 2025 Elsevier Inc. All rights are reserved, including those for text and data mining, AI training, and similar technologies.
https://doi.org/10.1016/j.matt.2025.102470

CellPress

Please cite this article in press as: Liu et al., Electrical control of a metal-mediated DNA memory, Matter (2025), https://doi.org/10.1016/j.matt.2025.102470

Matter

CellPress

Article

Electrical control of a metal-mediated DNA memory

Bo Liu,[1,6] Brandon Lu,[2,6] Arpan De,[3] Kyoungdu Kim,[1] Lara Perren,[2] Karol Woloszyn,[2] Galina Petrova,[3] Ruihao Li,[1] Chu-fan Yang,[2] Chengde Mao,[4] Antia S. Botana,[5] Yoel P. Ohayon,[2] James W. Canary,[2] Ruojie Sha,[2] M.P. Anantram,[3,*] Simon Vecchioni,[2,*] and Joshua Hihath[1,7,*]

[1]Center for Bioelectronics and Biosensors, School of Electrical, Computer, and Energy Engineering, Arizona State University, Tempe, AZ 85287, USA

[2]Department of Chemistry, New York University, New York, NY 10003, USA

[3]Department of Electrical and Computer Engineering, University of Washington, Seattle, WA 98195, USA

[4]Department of Chemistry, Purdue University, West Lafayette, IN 47907, USA

[5]Department of Physics, Arizona State University, Tempe, AZ 85281, USA

[6]These authors contributed equally

[7]Lead contact

*Correspondence: anant@uw.edu (M.P.A.), sv1091@nyu.edu (S.V.), jhihath@asu.edu (J.H.)

https://doi.org/10.1016/j.matt.2025.102470

PROGRESS AND POTENTIAL The unique chemical programming capabilities of DNA have transformed it from a simple carrier of genetic information into a broadly functional nanomaterial, making it a central element in nanoengineered structures, materials, computational systems, and data-storage paradigms. Along these lines, DNA's potential for creating high-density, low-energy-cost information storage systems has garnered significant interest; however, retrieving data from these systems relies on sequencing techniques and remains incompatible with modern electronic systems, hindering scalability and real-time operation. In this paper, we demonstrate that DNA can be used as a fully electronic, chip-integrated ternary memory system. This system utilizes individual, metal-mediated DNA duplexes as an active unit to read, write, and erase digital data. The electrical state of a single thymine:thymine metal base pair within the DNA duplex is modulated by electrically gating the system to atomically position Ag^+ and Hg^{2+} ions in one of three distinct coordination states. The devices can be cycled reversibly, opening new avenues for electronic DNA-based data storage.

SUMMARY

We demonstrate that a single DNA duplex that is designed to allow binding to specific metal ions (Hg^{2+}/Ag^+) and <3 nm in length can function as a fully electronic multi-bit memory system (+1, 0, −1). The system is reversible, allowing digital information to be electrically written, read, and erased in a solid-state, chip-based platform. This demonstrates a method that can enable DNA-based systems to be integrated with conventional electronics at scale and to electrically control chemical reactions that allow the electronic structure within the DNA to be modified to store information.

INTRODUCTION

Moore's law has tracked the rapid expansion of information technologies since the early 1970s. However, in recent years, the continued size scaling of transistor structures has stalled. Gate lengths have hovered between 10 and 15 nm for 10 years now, while gate pitches remain around 45 nm.[1–4] Despite these restrictions, computing requirements in general, and memory requirements in particular, are expanding exponentially, with over 2.5 quintillion bytes of data being produced each day.[5,6] Given this demand and the associated costs of device production and energy consumption, new paradigms for molecular computing and memory storage are being explored.[7–9]

Along these lines, the unique addressability, programmability, and structural recognition capabilities of DNA have led to its emergence as an important material programming system capable of technological functions far beyond its biological role, including the development of DNA nanotechnology and nanostructures, DNA-based computing and memory storage, and electronics.[2,10–15] In particular, its use as a system for digital memory storage has emerged as an intriguing possibility for high-density, long-term storage of digital information.[12,16–18] While massive storage densities can be achieved using solution-phase DNA, the information stored in the DNA must be extracted by sequencing the DNA molecules of interest, and it is difficult to extract this information quickly, reliably, and in a format that is straightforward to integrate with conventional

All rights are reserved, including those for text and data mining, AI training, and similar technologies.

Please cite this article in press as: Liu et al., Electrical control of a metal-mediated DNA memory, Matter (2025), https://doi.org/10.1016/j.matt.2025.102470

computers.[19–21] To be integrated with silicon-based computing technologies, memory elements should be dynamically read and written at fast timescales using electrical means.[22]

As a step toward integrating DNA memory approaches with conventional electronics, in this work we utilize metal-mediated DNA (mmDNA) as an electronic material and demonstrate that it can function as an all-electronic, single-molecule memory device capable of being written, read, and erased electronically. The electronic states of the system are modulated by using transition metal ion exchange in a T:T base pair at the center of a DNA duplex. This base pair (bp) can support three different coordination states of Ag^+ and Hg^{2+} ions as a function of environmental pH, in what is known as an mmDNA bp.[23–26] A single-molecule device is thus controlled to access the different coordination states by (1) directly changing the global pH through solvent exchange (chemical control) or (2) applying a gate voltage to modify the local pH in the immediate vicinity of the device (electrical control). We demonstrate that the states can be electrically cycled 48 times and that each state can be read over hundreds of cycles without failures. Reconfiguration of the metal ion states is validated using time-resolved crystallography, and the effects of the ion exchange upon the electronic structure of the DNA is determined using density functional theory (DFT) calculations and examination of the density of states (DoS) of the system. This system opens new approaches for developing DNA-based memories that are more compatible with conventional electronics and opens avenues for biosensing, ion detection, and neuromorphic applications.

RESULTS AND DISCUSSION

Development of metalated DNA-based electronic circuits

The primary active unit of the DNA-based memory is a single T:T mismatch at the center of a 9-bp DNA duplex that can support Ag^+/Hg^{2+} ions in lieu of a Watson-Crick hydrogen-bonding system (Figure 1).[23,27,28] Critically, two coordination sites exist in this pyrimidine-pyrimidine bp, mimicking the geometry of an A:T pair. At pH 8.0[29] the T:T pair will support two Hg^{2+} ions, at pH 11.0 it will coordinate two Ag^+ ions, and near the pK_a value of T (pH 9.5) it will support one of each ion, rendering this mmDNA pair a trinary memory system with states trivially labeled [−1], [0], and [1] for pH 8.0, 9.5, and 11.0, respectively (Figure 1A). The DNA duplex is synthesized with terminal C6-amine linkers, which are subsequently conjugated to carboxylic acids at the ends of metallic single-walled carbon nanotubes (mCNTs) that act as electrical leads by as described previously (see methods).[30–33] The mCNT-DNA-mCNT complexes are then drop cast onto a nanofabricated circuit with 32 pairs of gold electrodes, each with a junction gap of 300 nm (Figures 1 and S1) and a cysteamine self-assembled monolayer, to form single-molecule junctions. After incubation, each device is kept in a buffered environment and tested electrically to verify device formation and determine the conductance (G) and current-voltage (I-V) characteristics.

We first test the effects of the metal coordination state of the mmDNA on the overall electrical properties of the system. To establish a baseline, we initialize the molecular junctions in each coordination state during annealing and measure the ensuing conductance on chip. We measure a minimum of ten devices in each condition, with an overall yield of 22% across six chips (42/192 electrode pairs) (Figures 2A and S2). The conductance of each of the three configurations is different, and there is a systematic increase in the conductance as Hg^{2+} ions are substituted by Ag^+ ions. There is a 6-fold increase from $[Hg^{2+}]_2$ (state −1), to $[Ag^+]_2$ (state 1) ($G_{[Hg2+]2} = 6.51 \times 10^{-4}\ G_0$, $G_{[Hg2+][Ag+]} = 8.91 \times 10^{-4}\ G_0$, and $G_{[Ag+]2} = 2.17 \times 10^{-3}\ G_0$, where G_0 is the conductance quantum, $1G_0 = 77.48\ \mu S$). By contrast, the control sequence with an A:T pair at the center remains constant across these pH values ($8.1 \times 10^{-5}\ G_0$, Figure S3). This metal-ion-dependent conductance difference is also visible in the I-V traces (Figure 2B), indicating that metal ions significantly impact the electronic energy structure of the DNA. We characterized the devices using scanning electron microscopy (SEM) (Figure 1D) and Raman spectroscopy (Figure S1B), and we further performed control experiments before and after the addition of the chelating agent EDTA remove the metals from the DNA (supplemental methods and Figure S3). These experiments indicate the single-molecule nature of the devices and demonstrate that the nucleobase-bound transition metal ions are the key influence over the observed differences in conductance.

To understand why changes in individual atoms within the DNA stack led to significant alterations in the electronic properties of mCNT-DNA-mCNT devices, we conducted DFT calculations of the device structures to compare each of the three different configurations and compute the local DoS for each as a function of both energy and DNA length (Figure 2C; see DFT calculations). Because the conductance of G:C-rich DNA molecules is relatively high compared to shorter highly conjugated molecules such as oligo-phenylene-ethylene ([OPE]$\sim 1.2 \times 10^{-4}\ G_0$ OPE),[34] the conductance takes place over a length scale (~3 nm) where tunneling probability is low. As it has been shown that the conductance changes linearly (or nearly so) with changes in the molecular length,[35] charge transport in these systems is often ascribed to either a hopping or coherence-corrected hopping mechanism.[36] As such, we focus on examining the 2D DoS, which shows both the spatial delocalization and the energy separation of the molecular orbitals within the molecule, to examine the differences in the electronic structure and the potential for sequential hopping through the system. In this discussion, we assume that the highest occupied molecular orbital (HOMO) is close to the expected Fermi level of carbon nanotubes (CNTs) (~4.7 eV)[37,38] in all three configurations. We observe that the $[Hg^{2+}]_2$ case (state −1) shows a larger energy gap between HOMO and HOMO-1. Furthermore, since the HOMO is localized on one end of the molecule, this suggests a lower efficiency of charge transport via hopping. In contrast, the mixed $[Hg^{2+}][Ag^+]$ case (state 0) has a similar HOMO energy, but the presence of additional states near the HOMO energy enhances delocalization, which would enable higher probability of hopping between sites. The $[Ag^+]_2$ case (state 1) demonstrates a significant increase in both the number of energy levels and the overall DoS near the Fermi energy of the CNT. These findings highlight the potential for HOMO-mediated charge transport in these metalated DNA motifs and are consistent with the observed changes in the conductance values observed

Please cite this article in press as: Liu et al., Electrical control of a metal-mediated DNA memory, Matter (2025), https://doi.org/10.1016/j.matt.2025.102470

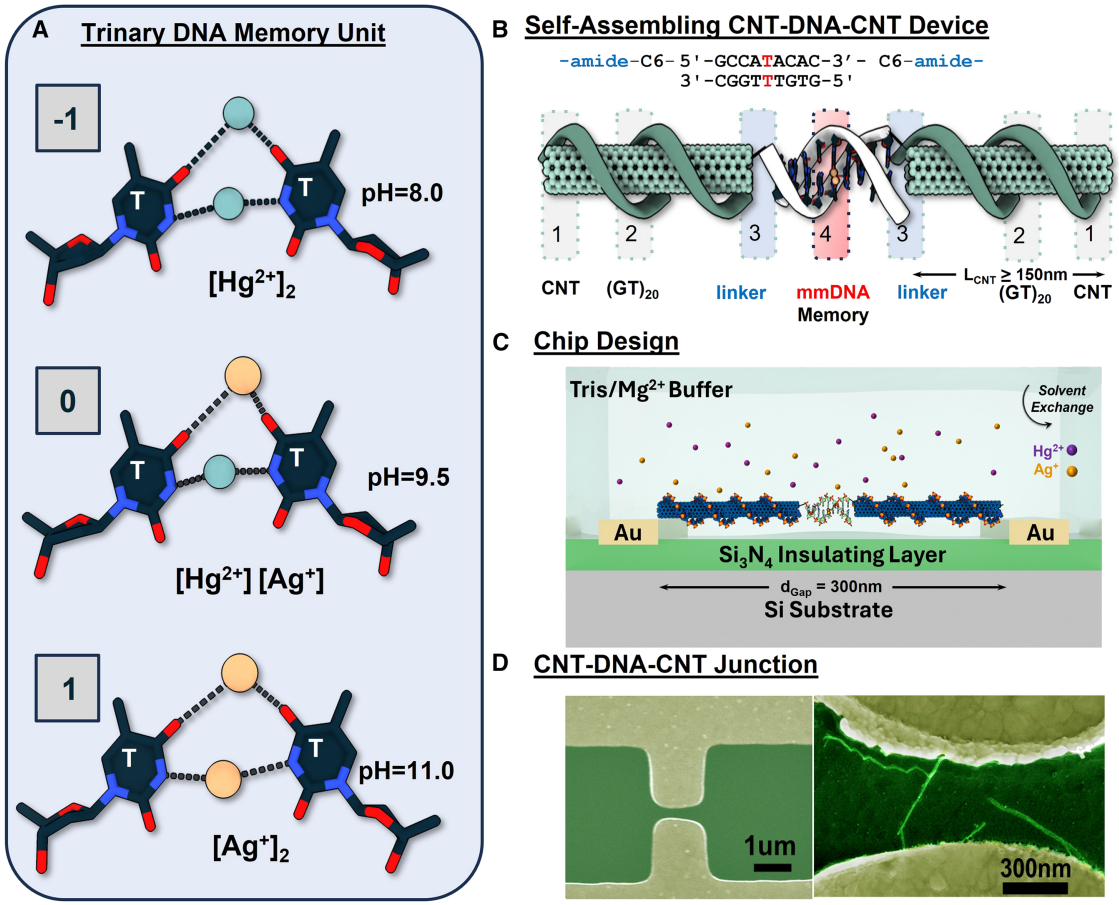


Figure 1. Architecture of a trinary DNA-based memory system

(A) A T:T mismatch exhibits a pH-dependent preference for Ag^+ and Hg^{2+} ions, leading to the formation of three distinct DNA memory states labeled −1, 0, and 1.

(B) Schematic diagram of a self-assembled junction, composed of (1) metallic nanotubes (2) wrapped in single-stranded $(GT)_{20}$ DNA, (3) covalently coupled by amine linkage to (4) a 9-bp DNA duplex with the T:T memory unit at the center.

(C) Schematic of an mCNT-DNA-mCNT nanojunction drop cast onto cysteamine-modified gold electrodes to create robust single-molecule junctions.

(D) SEM micrographs showing a standard 300-nm device and one with a single entity bridging the electrodes (both images shown in false color for clarity).

experimentally if a hopping-dominated transport mechanism is assumed.

In situ reconfiguration of ternary DNA memory

Having established both the single-molecule nature of the devices and the role of ion coordination in the transport properties, we next examine how changes in the solution pH can modify these states *in situ*, potentially enabling multi-bit storage functionality. To perform these experiments, we exchange the buffer solutions on chip from pH 11.0 to pH 8.0 to obtain $[Hg^{2+}]_2$, from pH 8.0 to 9.5 for $[Hg^{2+}][Ag^+]$, and from pH 9.5 to 11.0 for $[Ag^+]_2$ (see characterization section). Figure 3A shows an example of the changes obtained on a single device. To begin, the CNT solution is removed and replaced with the initial buffer at pH 9.5. The buffer solution is then systematically exchanged in the following order: pH 9.5 → 11.0 → 8.0 → 9.5 → 11.0, while a 0.5 V bias is applied to the device. As seen in Figure 3A, the conductance starts from 7.82×10^{-4} G_0 at pH 9.5 (state 0), then increases to 3.52×10^{-3} G_0 at pH = 11 ($[Ag^+]_2$, state 1). When decreasing to pH 8.0 directly from 11.0, we observe the appearance of an intermediate state with a conductance of 7.67×10^{-4} G_0 for ~10 s, consistent with a transit through state 0, before the conductance finally decreases to 5.22×10^{-4} G_0, in line with $[Hg^{2+}]_2$ coordination (state −1). The appearance of intermediary states, and the discrete changes in the conductance between the states, reinforces both the single-molecule and the single-ion-based operation of this device. If this were an ensemble measurement, the ion-replacement process would be stochastic across a large number of devices in the junction, leading to a continuous change in the conductance over the average ion-replacement time. To demonstrate full reversibility of the system, we then return the device to pH 9.5 and then pH 11.0 to obtain conductance values of 7.76×10^{-4} G_0 and 3.44×10^{-3} G_0, respectively. To further corroborate the *in situ* reconfigurability and reversibility of this system, we complete two full cycles of the pH exchange across four individual junctions. Each of the devices successfully underwent the exchanges without significant degradation of the conductance values (Figure 3B).

Please cite this article in press as: Liu et al., Electrical control of a metal-mediated DNA memory, Matter (2025), https://doi.org/10.1016/j.matt.2025.102470

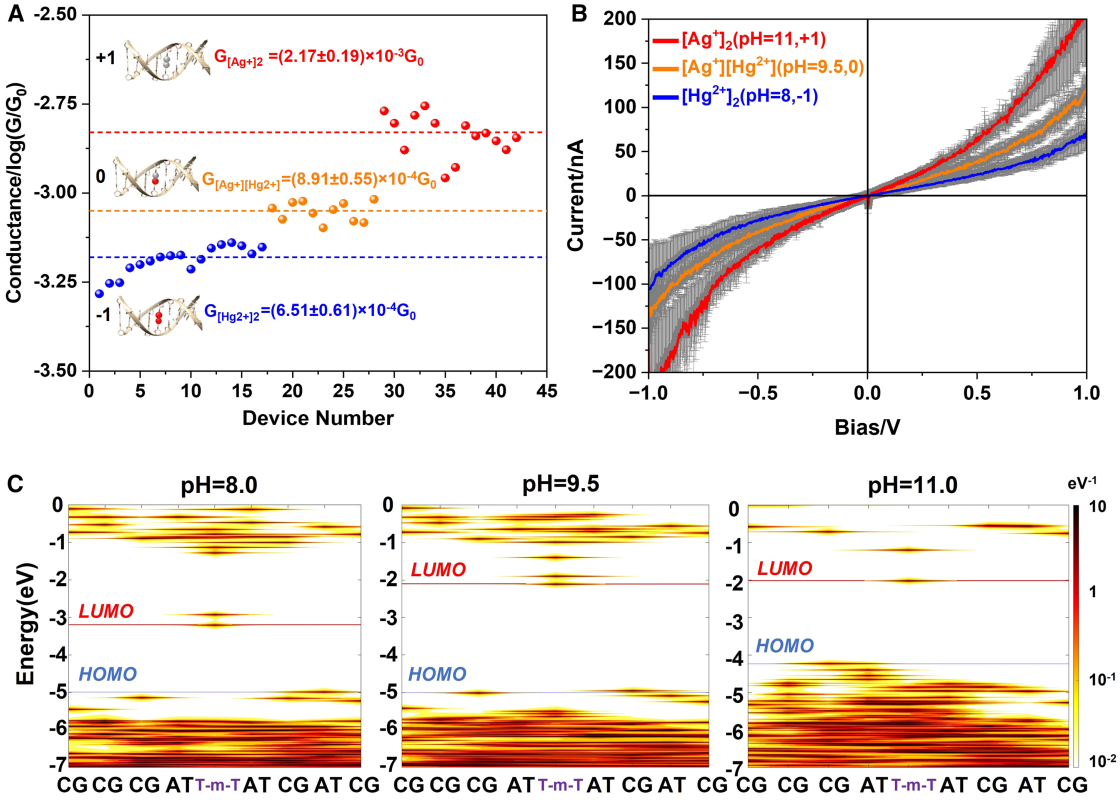


Figure 2. Electronic properties of metalated DNA

(A) Conductance values obtained for DNA duplexes prepared at different pH values. 17 devices at pH 8.0 in the $[Hg^{2+}]_2$ state show an average conductance of $6.51 \times 10^{-4}\,G_0$, 11 devices at pH 9.5 in the $[Hg^{2+}][Ag^{+}]$ state yield an average conductance of $8.91 \times 10^{-4}\,G_0$, and 14 devices at pH 11.0 in the $[Ag^{+}]_2$ state yield an average conductance of $2.17 \times 10^{-3}\,G_0$.

(B) Averaged *I-V* characteristics from all of the devices (each curve represents averaged *I-V* data from four scans per device, across 14, 11, and 17 devices for $[Ag^{+}]_2$, $[Hg^{2+}][Ag^{+}]$, and $[Hg^{2+}]_2$ states, respectively) at each pH value shown in (A). Error bars represent standard deviation.

(C) Base-pair-resolved density of states (DoS) contour plots and total DoS (lower panels) for the three experimental conditions: pH 8.0 ($[Hg^{2+}]_2$ system, left), pH 9.5 ($[Hg^{2+}][Ag^{+}]$ system, middle), and pH 11.0 ($[Ag^{+}]_2$ system, right). The *x* axis represents each of the 9 bps, with "T-m-T" indicating the metalated site. The LUMO is marked by a red line, while the HOMO level is indicated by the blue line. DoS values are plotted on a logarithmic scale.

To further validate the conductance switching processes and the kinetics of the ion exchange in the system, we perform *in situ* ion exchange experiments in self-assembling DNA crystals with the device sequence operating as one of the arms of the 3D triangle motif.[39] Crystals are grown at a specific pH value (8.0, 9.5, 11.0) and moved into metalated cryosolvent of a different pH. Atomic reconfiguration was captured by quenching crystals in liquid nitrogen at specific time points after exchange, followed by X-ray diffraction at synchrotron sources and structure determination by anomalous dispersion techniques. Here, we tested a variety of metal conditions in the cryosolvent, the scale of the pH change, and a wide range of reaction times, each yielding a separate molecular structure. The results of a full cycle, calibrated to the on-chip buffer conditions and carried out across many crystals, is shown in Figure 3C, with time resolution of a similar order to the conductance data. We note that the crystallographic data are diffusion limited, especially at short timescales, and represent an aggregate measurement across picomoles of devices. With that in mind, observation of time-resolved transmetalation in the same general speed as on-chip single molecules is notable. With bulk ion concentrations matching the on-chip measurements, all state transitions are rapid except the $[Hg^{2+}][Hg^{2+}]$ (state −1) to $[Hg^{2+}][Ag^{+}]$ (state 0) transition, which takes over 30 s—even in the absence of Hg^{2+} in the cryosolvent. Transmetalation reactions are carried out over slower timescales when crystals are moved from pH extremes, with the state [−1] to state [1] transition taking 90 s. The reverse reaction is not obtained in one step: crystals moved from pH 11.0 to pH 7.0 become stuck at state [0] after 300 s, repeated across all tested buffer conditions (Figures S4 and S5). These dynamics underscore the critical role of local millimolar-scale ion concentrations imposed by the solid-phase internal surface of tensegrity triangle crystals. Ions that diffuse away are still local to the bp, as evidenced by F_o-F_c difference maps with minor groove density at the O2 sites.[23] Local concentrations on the surface of the CNT device are, by contrast, similar to the bulk. Alternatively, transmetalation reactions carried out in pH increments of 1.5 units, both with and without Hg^{2+} in the cryosolvent, achieve successful reactions in time steps that complement on-chip switching (Figure 3D and Tables S2–S7). These data, and the repeatability

Please cite this article in press as: Liu et al., Electrical control of a metal-mediated DNA memory, Matter (2025), https://doi.org/10.1016/j.matt.2025.102470

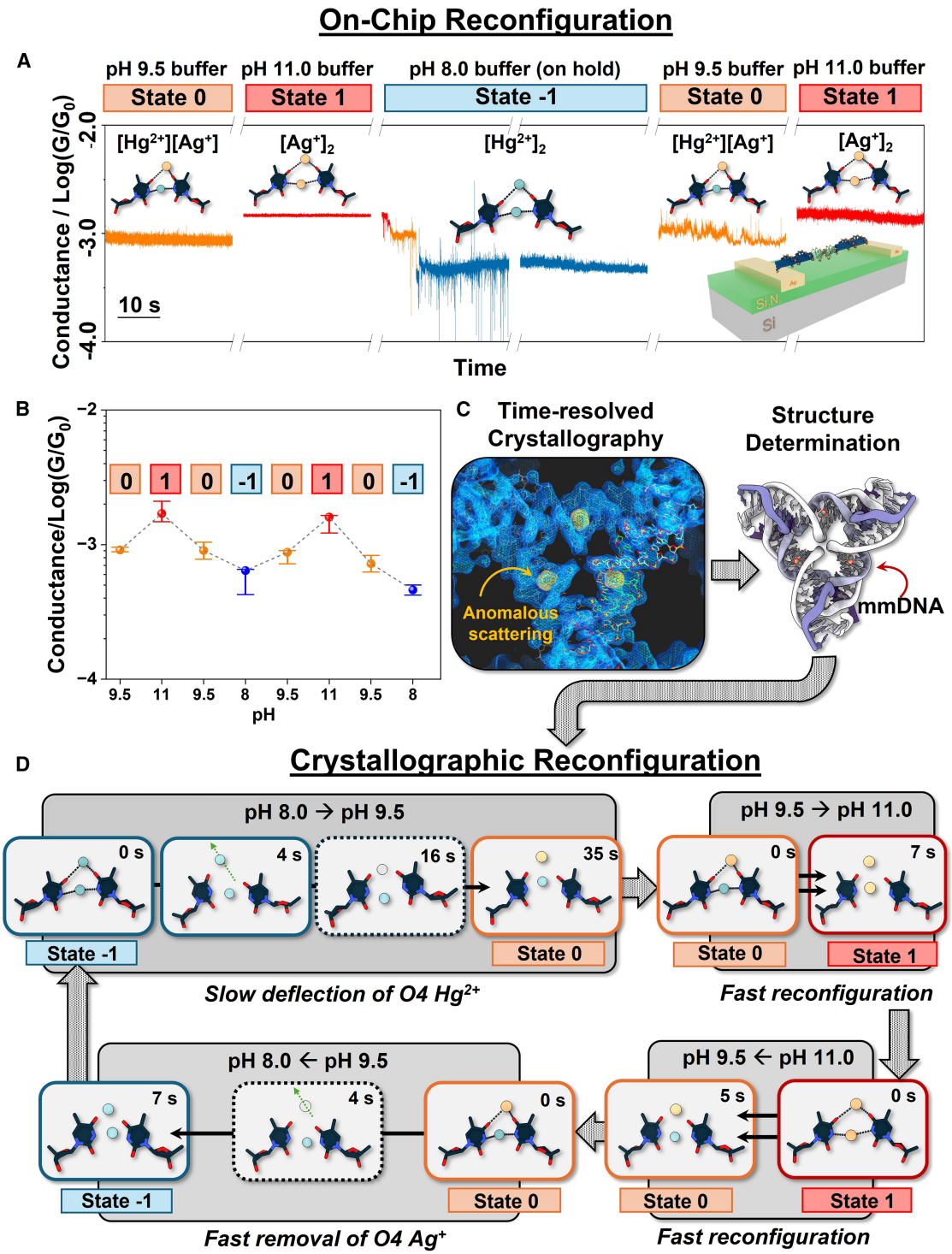


Figure 3. pH-based reconfiguration of metalated DNA structures

(A) Current vs. time trace for *in situ* modulation of the system pH for a single mCNT-DNA-mCNT device. As the pH is changed, the conductance tracks the steps seen in the static pH experiments, indicating ion replacement.

(B) Conductance values as a function of pH over eight solvent exchange cycles. Each of the devices continued functioning after switching. Data are average conductance values for seven devices measured over all cycles. Error bars represent standard deviation.

(C) Time-resolved crystallography of mmDNA bps.

(D) Crystal structures are obtained using *in situ* studies of self-assembling DNA crystals containing the device sequence. A full cycle, from 8.0 → 9.5 → 11.0 → 9.5 → 8.0, is obtained *in crystallo*, with each time point representing a difference in crystal structure.

Please cite this article in press as: Liu et al., Electrical control of a metal-mediated DNA memory, Matter (2025), https://doi.org/10.1016/j.matt.2025.102470

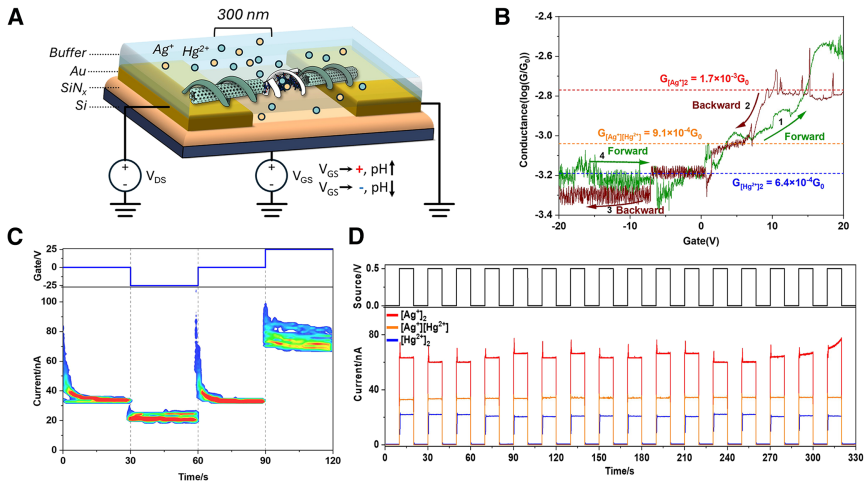


Figure 4. Electrically controlled DNA-based memory operation

(A) Schematic of experimental setup. A heavily doped Si substrate is used as a back gate to control the surface pH.

(B) Typical current vs. gate response of a single metalated DNA nanostructure at a bulk pH of 9.5 (v_{scan} = 0.05 V/s, following the scan direction 1 → 2 → 3 → 4). At large positive gate voltages (high surface pH) the system stabilizes in the $[Ag^+]_2$ state, and at negative gate voltages (lower pH), the $[Hg^{2+}]_2$ is obtained. Near zero bias, the surface pH is dictated by the bulk pH, and the $[Hg^{2+}][Ag^+]$ state is observed.

(C) Example of directly writing the DNA memory states. By modulating the gate voltage (upper panel) to discrete values in individual steps, specific device states can be obtained. Lower panel displays a histogram of 12 complete write cycles of four states, representing 48 conductance switches for a single device.

(D) Bias cycling for the system. The gate voltage is set at three specific gate voltages, and a square wave potential is applied to the source-drain bias. Sixteen bias cycles are applied for each state, representing a total of 48 read cycles for a single device.

across reaction conditions, demonstrate the feasibility of rewriting mmDNA conductance states through pH-induced metal ion exchange.

Electrical control of ternary DNA memory

Given that the significant changes in electrical response of the mmDNA systems that occur with pH control are comparable with some modern multi-level memory systems,[40,41] we next aim to determine whether these states can be accessed by electrical control. To enable electrical control of the device states, we implement the system on the highly doped silicon substrate, separated from the mCNT-DNA-mCNT junction by 300 nm of Si_3N_4, to function as a back gate to control the surface pH and the competition reaction between the Ag^+ and Hg^{2+} ions (Figures 4A and 4B).[42–47] These experiments are performed in a solution containing $AgNO_3$ and $HgCl_2$ without a buffering compound in order to allow maximum control over the surface pH. Applying the Gouy-Chapman-Stern (GCS) model to our device structure with a bulk pH value of 9.5 (state 0), we estimate that a gate range of ±20 V will allow the surface pH to be controlled over a range of 7.8–11.1 (Figure S6).[48–50] Initial gating experiments are performed by measuring the source-drain current (I_{SD}) while the bias (V_{SD}) is held constant (0.5 V) and the gate voltage (V_g) is swept over a range of ±20 V (Figure 4B). We note that the change in conductance with gate control is not uniform but is marked by discontinuities that are consistent with the device switching between each of the three conductance states for the device. Above +15 V we obtain a conductance value for the $[Ag^+]_2$ state (state 1), below −10 V the $[Hg^{2+}]_2$ state (state −1) predominates, and near 0 V we obtain the baseline $[Hg^{2+}][Ag^+]$ coordination (state 0). The observed hysteresis likely reflects kinetic limitations in ion exchange, with diffusion delays contributing to slight differences between forward and backward sweeps. Gating experiments on a DNA sequence without a T:T bp in the same environment showed very limited gate effects (Figure S7), and pH changes with only a single metal ion present in solution did not result in significant conductance changes (Figure S8), thus indicating that the gate-induced pH changes are enabling the ion-exchange process. Next, to test device writing fidelity and demonstrate that each of the three memory states in this ternary system can be electrically accessed independently, we systematically step the gate voltage in a square wave cycle from 0 → −25 V → 0 V → +25 V. This cycle is repeated 12 times to obtain 48 switching events for one single device, and a histogram of the measured currents over this entire process is shown in Figure 4C, whereas the retention times extracted from each state change are shown in Figure S9. Of particular note is the small dispersion in current values obtained at each gate voltage, clearly indicating the fidelity, reproducibility, and stability of both the states and the system as a whole.

Finally, to demonstrate the stability of these states, we perform systematic read cycles at each of the gate voltages. For three different gate voltages (25, 0, and −25 V), we apply a square wave voltage to V_{SD} that oscillates between 0 V and 0.5 V with a frequency of 0.1 Hz and a duty cycle of 50%. Figures 4D and S10 show examples of single devices operated at each gate voltage for 16 read cycles, yielding a total of 48 bias cycles on a single molecular junction, demonstrating stable operation of this volatile DNA-based memory element.

This work demonstrates an alternative paradigm for advancing DNA-based memory systems, enabling these systems to be directly integrated with, controlled by, and read by electronic devices. In this architecture, control over two atomic binding sites is achieved by modulating a local electric field, creating a reliable and adaptable ternary DNA memory element that directly integrates with existing electronic infrastructure while maintaining molecular-level precision. This DNA-based nanoarchitecture permits multiple logical states within a single memory unit, increasing information density compared to conventional binary systems. We emphasize that the composable elements of this system are based on unmodified nucleobases with easily accessible chemistry. Thus, by expanding to incorporate greater numbers of configurable metal ions and coupling different mmDNA bps with tunable coordination and pK_a values, those

Please cite this article in press as: Liu et al., Electrical control of a metal-mediated DNA memory, Matter (2025), https://doi.org/10.1016/j.matt.2025.102470

nanostructures will be widely enabling of more complex electronic DNA memory and logic systems, benefiting not only electrically driven DNA computing and digital logic but also offering potential for neuromorphic computing applications. These results open up avenues for continued scaling and leveraging of the inherent nanoscale control of DNA structures for next-generation information storage media.

METHODS

Preparation of mCNT-DNA-mCNT nanostructures

The mCNT wrapping process is driven primarily by favorable interactions between the single-stranded DNA (ssDNA) bases and the mCNT due to van der Waals and hydrophobic interactions. 0.1 mL of the mCNT (1 mg/mL, with sodium dodecyl sulfate [SDS] and sodium lauryl ether sulfate [SLES]) surfactants) solution is first diluted with 2.5 mL of dulbecco's phosphate-buffered saline [DPBS], then 2.5 mL of 5 μM $(GT)_{20}$ is added. After overnight incubation at room temperature, the mixture is placed in a clean tube surrounded by ice for at least 2 h under sonication (at the power level of 3 W), which is then centrifuged at 5,000 rpm (Eppendorf 5415C) for 2 h to remove insoluble material. The supernatant is collected and diluted with deionized (DI) water (Milli-Q) and the volume of $(GT)_{20}$-dispersed mCNT solutions kept to 2 mL.

To covalently attach mDNA duplexes to $(GT)_{20}$ wrapped mCNTs, we begin with amino-terminated DNA prepared at a concentration of 5 μM in 2 mL of PBS buffer and mix it with 2 mL of $(GT)_{20}$ wrapped mCNTs and ~0.13 mM hexafluorophosphate azabenzotriazole tetramethyluronium (HATU, coupling agent with surfactant).[30] The mixture is left to react at room temperature for 3 h under weak sonication. Subsequently, any insoluble material is removed via 15 min of centrifugation at 12,000 rpm. The mCNT-DNA-mCNT hybrids are then extracted from the supernatant and readied for transfer onto nanofabricated Au electrodes with 300-nm gaps.

Nanoelectrode array fabrication and single-molecule junction integration

The microelectrode platform used for electrical tests of the nanostructures was fabricated by using standard lithography techniques. In brief, a Si/low-pressure chemical vapor deposition (LPCVD)-Si_3N_4 wafer is first spin coated with hexamethyldisilazane (HMDS) as an adhesive layer, followed by PID-controlled baking at 180°C for 1 min. Microelectrodes are then patterned on the wafer using photolithography with a KL5302 hi-res photoresist (Kem Lab) and LOR 3A as a lift-off layer (Kayaku). After ~20 s of development in CD-26 (TMAH), the wafer is gently rinsed with DI water and blow-dried with nitrogen to stop the development process. A polymer etch transfer using reactive ion etching (PET-RIE) plasma etcher is then employed to etch ~60-nm trenches into silicon nitride. A Cr (adhesive)/Au multilayer of thickness 5 nm/65 nm is deposited by an e-beam evaporator (Lesker). The sample is then immersed in Removal PG (Kayaku) for 90 min and ultrasonicated to lift off residual resist and metal. After that, a 100-nm-thick Si_3N_4 insulating layer is deposited using plasma-enhanced chemical vapor deposition (PECVD) to cover the gold electrodes. Micrometer-sized windows for the probing and sensor areas are patterned using the same photolithography process used previously for the microelectrodes. Finally, a ~110-nm etch into the PECVD Si_3N_4-cover layer is performed using a Plasma-Therm RIE to open the windows and expose the gold electrodes in the desired areas.

To couple the mCNT-DNA-mCNT structures to the Au electrode surfaces, we began by immersing the freshly made substrates in a 0.5 mM solution of cysteamine overnight after 5 min of UV-ozone treatment. The substrates were then removed from the solution, gently rinsed with DI water, and dried with a stream of nitrogen gas. After device characterization (blank test), a Teflon ring was mounted and sealed to the sensor area as a sample reservoir. Thereafter, the mCNT-DNA-mCNT nanostructures were incubated on-chip in a 100 mM Tris buffer solution to bridge the gaps and create a mechanically robust device.

Characterization

All electrical device characterization is performed using a Cascade micromanipulator probe station equipped with a precise XYZ three-axis stage at room temperature. Current signals are collected by MCC1808X DAQ with a lab-designed transimpedance amplifier. Each electrode underwent current sampling at 0.5 V bias for a minimum of 3 min, followed by voltammetry scanning over a range from −0.5 V to 0.5 V.

Bare silicon (12 mm × 12 mm × 280 μm) serves as backside gate electrode and is connected to a programmable voltage output channel. To ensure that any unattached or nonspecifically bound molecules are completely removed during the sample exchange, we pipette out the solution and then rinse the sample reservoir with buffers before introducing a new sample.

X-ray diffraction

Sample preparation

Oligonucleotides were purchased from Integrated DNA Technologies (Coralville, IA, USA) with standard desalting. Strands with amino modifications were synthesized on an Applied Biosystems 394 automatic DNA synthesizer, cleaved from solid support and deprotected in ammonium hydroxide for 24 h at room temperature, and dried at 55°C according to routine phosphoramidite protocols. Sequences can be found in Table S1. Strands were purified using denaturing PAGE containing acrylamide (19:1 acrylamide/bisacrylamide), TBE buffer (40 mM Tris, 40 mM boric acid, and 2 mM EDTA), and 50% urea by mass running at 600 V for 1 h. After running, gels were stained with ethidium bromide (EtBr), and corresponding bands were excised under UV illumination. DNA was eluted in buffer solution containing 500 mM ammonium acetate, 10 mM magnesium acetate, and 1 mM EDTA at 4°C overnight. 1-Butanol was used to extract the eluate in order to remove EtBr, and DNA was recovered with ethanol precipitation. Final concentration of DNA resuspended in double-distilled water was estimated with optical density (OD) at 260 nm using an IMPLEN P300 nanophotometer.

Crystals were grown in 10-μL hanging drops of 36 μM helical and crossover-strand DNA and 12 μM center-strand DNA in 40 mM Tris, 125 mM magnesium sulfate, 24 μM $AgNO_3$, and 48 μM $HgCl_2$ at pH 8.0, 9.5, and 11.0 (adjusted with 1 M sodium hydroxide and/or 10% sulfuric acid) equilibrated against 400 mM Tris and 1.25 M magnesium sulfate. Crystals were heated to

Please cite this article in press as: Liu et al., Electrical control of a metal-mediated DNA memory, Matter (2025), https://doi.org/10.1016/j.matt.2025.102470

65°C at 5°C/h and cooled down to 20°C at a rate of 0.4°C/h. After ~7 days, crystals were observed under light microscopy and images were taken. Single crystals were picked up using a crystal loop and placed into cryoprotectant solution (280 mM Tris, 875 mM magnesium sulfate, 16.8 μM $AgNO_3$, and 33.6 μM $HgCl_2$) at pH 9.5, 11.0, and 8.0 for the specified time frames before plunging into liquid nitrogen.

Crystals were diffracted at the Advanced Photon Source at Argonne National Laboratory (IMCA-CAT, beamline 17-ID) as well as the National Synchrotron Light Source II at Brookhaven National Laboratory (AMX, FMX, beamlines 17-ID1,2). Diffraction occurred at or above the L-III peak of Hg (12,307 eV, 1.0074 Å). Diffraction images were indexed and integrated using autoPROC software (Global Phasing). STARANISO was used to correct for anisotropy and increase resolution with an elliptical cutoff. Structure solution was carried out in Phenix with molecular replacement (search model PDB: 5W6W modified to include T-T pairs at the center of the asymmetric unit) and single-wavelength anomalous dispersion (SAD). Metal ions were placed using Autosol, and occupancies were then refined using F″ refinement. Structures were deposited to the PDB (accession codes PDB: 9MM7, 9MM8, 9MM9, 9ND7, 9ND6, 9ND8, 9ND9, 9MMA, 9MMB, 9MMC, 9MMD, 9MM3, 9MM4, 7TG4, 7TF6, 7TG7, 7TG8, 7TG9, 7TGA, 7TGB, 7TGC, and 7TGD). Diffraction tables can be found in the supplemental information.

Raman spectroscopy

CNT samples were characterized using Raman spectroscopy (WITec) equipped with a 532-nm laser source. The laser power was maintained at 1.0–2.0 mW to prevent sample heating and potential damage to the CNT structure. Measurements were conducted at room temperature (23°C ± 1°C) under ambient conditions. Raman spectra were acquired in the range of 0–3,000 cm^{-1} with a spectral resolution of 1 cm^{-1}. For each sample, measurements were taken at five different locations to ensure reproducibility. The exposure time was set to 20 s with three accumulations per spectrum to optimize signal-to-noise ratio. The laser spot size was approximately 1 μm in diameter. Peak deconvolution was performed using OriginPro software.

DFT calculations

The 9-mer mmDNA structures were constructed by extracting 7-mer mmDNA segments from the broader tensegrity triangle crystal frameworks with COOT v.1.1[51] followed by the incorporation of terminal GC clamps in COOT, and the backbone was terminated using the t leap utility in AMBER.[52] At high pH (>9.0), we removed the hydrogens from the thymine, while at low pH (≤9.0), the N3 coordinated hydrogen of the thymine was moved to neighboring O4 atoms.[53] Gaussian 16 is used for all DFT modeling.[54] A mixed-basis setup was adopted with LANL2DZ basis set for metal atoms and 6-31g(d,p) basis set for non-metal atoms. The B3LYP functional was used in all calculations with the polarizable continuum model to account for the solvent (water) effect. The default convergence criterion ($<10^{-8}$) was considered for self-consistent field (SCF) calculations. As the modeled structures consist of more than 600 atoms, we adopted a partial DFT optimization technique. In the first step, we performed a force calculation to locate the atoms with force above a threshold of 3 eV/Å. The locations of these atoms alone were optimized with the constraint that the atoms with low forces were frozen. The forces were calculated again, and the optimization process was repeated until atoms had a force lower than the threshold of 3 eV/Å. With the optimized structure of each DNA strand, we performed a single-point DFT calculation to find the Hamiltonian (H_{DNA}) of the DNA that had been used for further analysis.

DoS calculations

Following DFT calculations in Gaussian, we extracted the system Hamiltonian by applying the Löwdin transformation:

$$H_{DNA} = S^{-1/2} F S^{-1/2}, \quad \text{(Equation 1)}$$

where F and S are Fock and overlap matrices.

The DoS due to a specific orbital on an atom, which is jointly defined by index p, is calculated by solving the following equations ($\eta = 0.001$):

$$[(E + i\eta) - H_{DNA}]G^r = I, \quad \text{(Equation 2)}$$

where E is the energy, $i\eta$ is imaginary term (η is positive and small) used to avoid singularities in the Green's function, and H_{DNA} is the Hamiltonian of DNA. Next, we calculate DoS by extracting the corresponding diagonal elements of Green's function as follows:

$$\mathrm{DoS}(p,E) = -\frac{1}{\pi} Im(G^r(p,p,E)). \quad \text{(Equation 3)}$$

Here, DoS(p,E) is the local density of states at (atom, orbital) p and energy E. $G^r(p,p,E)$ is the retarded Green's function at (atom, orbital) p and energy E.

Local pH estimation: GCS model

The GCS model[48,55] is a theoretical framework used to describe the electrical double layer (EDL) at the interface between a charged solid surface (like a metal or semiconductor) and an electrolyte solution. To estimate surface pH around a bridged mCNT-mDNA junction, we first determine EDL thickness (Stern layer thickness + Gouy-Chapman layer). The Stern layer thickness estimation is approximately 0.3–0.5 nm; here we use (d = 0.4 nm).

The Gouy-Chapman (diffuse) layer thickness (Debye length λ_D) estimation is[55]

$$\lambda_D = \sqrt{\frac{\varepsilon_r \varepsilon_0 k_B T}{2 N_A e^2 I}}.$$

Here, ε_r is relative permittivity of solution at 25°C (≈78.5), ε_0 is vacuum permittivity (8.854×10^{-12} F/m), k_B is Boltzmann's constant (1.380649×10^{-23} J/K), T is 298 K, N_A is Avogadro's number (6.022×10^{23} mol^{-1}), e is elementary charge (1.602×10^{-19} C), and I is ionic strength of the solution (mol/L).

Please cite this article in press as: Liu et al., Electrical control of a metal-mediated DNA memory, Matter (2025), https://doi.org/10.1016/j.matt.2025.102470

The ionic strength of the solution is

$$I = 0.5\sum_i C_i \times z_i^2,$$

where C_i is the molar concentration of ion i, and z_i is the charge number of ion i.

Then, as the charge density at the inner Helmholtz plane (IHP) ((σ_{IHP}) is directly proportional to the applied gate voltage (V_g), charge density at the IHP is linearly dependent on gate voltage for this example. Considering (1) the gate voltage (V_g) is distributed across the SiNx layer and the Stern layer, and (2) the surface-side charges (σ_{eff}) are exactly counterbalanced by the diffuse layer charges ($\sigma_d(\psi_d)$),

$$\sigma_{eff} = \sigma_d(\psi_d),$$

$$\sigma_{eff} = \sigma_{sites} + \sigma_{IHP} = e\Gamma(\alpha f^+ - f^-) + \frac{C_{SiNx}}{C_{SiNx}+C_{Stern}}V_g,$$

$$C_{SiNx} = \frac{\varepsilon_0\varepsilon_r}{d},$$

where σ_{sites} is the surface charge density from ionized sites (C/m^2), α is the ratio of amine sites ($SiNH_2$) to silanol sites (SiOH) on the surface (0.013 for Si_3N_4), Γ is the total site density (value is 1.25×10^{18} sites/m^2), f^+ is the protonated amine fraction ($0 \leq f^+ \leq 1$, at pH 9.5 [close to pK_a = 10], $f^+ \approx 0.76$), f^- is the deprotonated silanol fraction ($0 \leq f^- \leq 1$, at pH 9.5 [well above pK_a = 6], $f^- \approx 1$), C_{SiNx} is capacitance of the SiNx layer (d_{SiNx} = 200 nm, $C_{SiNx} = 4 \times 10^{-4}$ F/m^2), and C_{Stern} is capacitance of the Stern layer (d_{Stern} = 0.4 nm, C_{stern} = 0.02 F/m^2).

To numerically solve the 1D Poisson-Boltzmann equation for the surface potential,[56,57] we assume a thin double layer (where the Debye length is significantly smaller than the system's dimensions).

$$\frac{d^2\psi(x)}{dx^2} = \frac{2n_0e}{\varepsilon}\sinh\left(\frac{e}{k_BT}\psi\right),$$

$$pH(x) = pH_{bulk} - \frac{e\psi(x)}{2.303k_BT}.$$

Using a Python script, we estimate the local pH as a function of gate voltage, ranging from −30 V to 30 V. These results are visualized in Figure S6.

RESOURCE AVAILABILITY

Lead contact

Requests for further information, resources, and reagents should be directed to and will be fulfilled by the lead contact, Joshua Hihath (jhihath@asu.edu).

Materials availability

This study did not generate new unique materials.

Data and code availability

All materials utilized in the experiment can be obtained from the principal investigator upon valid request. This study did not generate code.

ACKNOWLEDGMENTS

The authors acknowledge support from the National Science Foundation Growing Convergence Research (NSF-2317843), Future Manufacturing (NSF-2328217), Chemical Measurement and Imaging (NSF-2239226), and the Keck Foundation. This work was further supported by the Office of Naval Research (N000141912596) and the Office of Basic Energy Sciences in the Department of Energy (DE-SC0007991).

AUTHOR CONTRIBUTIONS

The research was conceptualized and the experimental framework designed by J.H., S.V., M.P.A., and B. Liu. B. Liu carried out single-molecule electrical testing and morphology inspections and collected the relevant data. B. Lu, L.P., K.W., C.-f.Y., C.M., and S.V. performed crystal growth and crystallographic analysis of the transmetalation reaction and handled data collection and analysis. K.K. was responsible for chip fabrication and inspection. R.L. performed Raman spectroscopy. A.D. and G.P. conducted DFT and DoS calculations. B. Liu conducted statistical analysis and created the visualizations. A.S.B., Y.P.O., J.W.C., and R.S. supplied critical reagents, materials, and technical expertise. B. Liu wrote the initial draft of the manuscript, with S.V. contributing to the crystallography sections. J.H. and M.P.A. provided essential revisions and intellectual input to refine the manuscript. All authors reviewed, edited, and approved the final manuscript for submission.

DECLARATION OF INTERESTS

The authors declare no conflict of interest.

DECLARATION OF GENERATIVE AI AND AI-ASSISTED TECHNOLOGIES IN THE WRITING PROCESS

No artificial intelligence (AI) tools or technologies were used in the preparation, writing, or editing of this paper.

SUPPLEMENTAL INFORMATION

Supplemental information can be found online at https://doi.org/10.1016/j.matt.2025.102470.

Received: June 6, 2025
Revised: August 12, 2025
Accepted: September 9, 2025

REFERENCES

1. Oehrlein, G.S., Brandstadter, S.M., Bruce, R.L., Chang, J.P., DeMott, J.C., Donnelly, V.M., Dussart, R., Fischer, A., Gottscho, R.A., Hamaguchi, S., et al. (2024). Future of plasma etching for microelectronics: Challenges and opportunities. J. Vac. Sci. Technol. B *42*, 041501.
2. Cao, W., Bu, H., Vinet, M., Cao, M., Takagi, S., Hwang, S., Ghani, T., and Banerjee, K. (2023). The future transistors. Nature *620*, 501–515.
3. Kim, K.S., Kwon, J., Ryu, H., Kim, C., Kim, H., Lee, E.-K., Lee, D., Seo, S., Han, N.M., Suh, J.M., et al. (2024). The future of two-dimensional semiconductors beyond Moore's law. Nat. Nanotechnol. *19*, 895–906.
4. Wang, W., Yi, S.D., Li, F., Cao, Q., Shi, J., Kang, B.-M., Jin, M., Liu, C., Wu, Z., Wang, G., and Zhao, C. (2024). Vertical Surrounding Gate Transistor for High Density and Low Voltage Operation in DRAM. IEEE Access *12*, 46504–46511.
5. Sardar, T.H., and Pandey, B.K. (2024). Big Data Computing: Advances in Technologies, Methodologies, and Applications (CRC Press)).
6. Khan, N., Yaqoob, I., Hashem, I.A.T., Inayat, Z., Ali, W.K.M., Alam, M., Shiraz, M., and Gani, A. (2014). Big data: survey, technologies, opportunities, and challenges. Sci. World J. *2014*, 712826.

Please cite this article in press as: Liu et al., Electrical control of a metal-mediated DNA memory, Matter (2025), https://doi.org/10.1016/j.matt.2025.102470

7. Liu, S., Huang, H., Li, Y., Zhang, Z., Zhang, Y., Li, Y., Wang, Q., Zhang, Q., Huo, J., Yao, J., et al. (2024). Reconfigurable Five-In-One Carbon Nanotube Optoelectronic Transistor for Intelligent Computing and Communication. ACS Appl. Mater. Interfaces *16*, 54435–54444.
8. Yan, A., Wang, C., Yan, J., Wang, Z., Zhang, E., Dong, Y., Yan, Z.Y., Lu, T., Cui, T., Li, D., et al. (2024). Thin-Film Transistors for Integrated Circuits: Fundamentals and Recent Progress. Adv. Funct. Mater. *34*, 2304409.
9. Si, J., Zhang, P., Zhao, C., Lin, D., Xu, L., Xu, H., Liu, L., Jiang, J., Peng, L.-M., and Zhang, Z. (2024). A carbon-nanotube-based tensor processing unit. Nat. Electron. *7*, 684–693.
10. Pan, C., Tabatabaei, S.K., Tabatabaei Yazdi, S.M.H., Hernandez, A.G., Schroeder, C.M., and Milenkovic, O. (2022). Rewritable two-dimensional DNA-based data storage with machine learning reconstruction. Nat. Commun. *13*, 2984.
11. Chen, K., Zhu, J., Bošković, F., and Keyser, U.F. (2020). Nanopore-based DNA hard drives for rewritable and secure data storage. Nano Lett. *20*, 3754–3760.
12. Yang, S., Bögels, B.W.A., Wang, F., Xu, C., Dou, H., Mann, S., Fan, C., and de Greef, T.F.A. (2024). DNA as a universal chemical substrate for computing and data storage. Nat. Rev. Chem *8*, 179–194.
13. Robinson, B.H., and Seeman, N.C. (1987). The design of a biochip: a self-assembling molecular-scale memory device. Protein Eng. *1*, 295–300.
14. Winfree, E., Liu, F., Wenzler, L.A., and Seeman, N.C. (1998). Design and self-assembly of two-dimensional DNA crystals. Nature *394*, 539–544.
15. Han, D., Pal, S., Nangreave, J., Deng, Z., Liu, Y., and Yan, H. (2011). DNA origami with complex curvatures in three-dimensional space. Science *332*, 342–346.
16. Fei, Z., Gupta, N., Li, M., Xiao, P., and Hu, X. (2023). Toward highly effective loading of DNA in hydrogels for high-density and long-term information storage. Sci. Adv. *9*, eadg9933.
17. Ceze, L., Nivala, J., and Strauss, K. (2019). Molecular digital data storage using DNA. Nat. Rev. Genet. *20*, 456–466.
18. Hoose, A., Vellacott, R., Storch, M., Freemont, P.S., and Ryadnov, M.G. (2023). DNA synthesis technologies to close the gene writing gap. Nat. Rev. Chem *7*, 144–161.
19. Li, K., Lu, X., Liao, J., Chen, H., Lin, W., Zhao, Y., Tang, D., Li, C., Tian, Z., Zhu, Z., et al. (2024). DNA-DISK: Automated end-to-end data storage via enzymatic single-nucleotide DNA synthesis and sequencing on digital microfluidics. Proc. Natl. Acad. Sci. USA *121*, e2410164121.
20. Wang, S., Mao, X., Wang, F., Zuo, X., and Fan, C. (2024). Data Storage Using DNA. Adv. Mater. *36*, 2307499.
21. Gervasio, J.H.D.B., da Costa Oliveira, H., da Costa Martins, A.G., Pesquero, J.B., Verona, B.M., and Cerize, N.N.P. (2024). How close are we to storing data in DNA? Trends Biotechnol. *42*, 156–167.
22. De, A., Mohammad, H., Wang, Y., Kubendran, R., Das, A.K., and Anantram, M.P. (2023). Performance analysis of DNA crossbar arrays for high-density memory storage applications. Sci. Rep. *13*, 6650.
23. Lu, B., Ohayon, Y.P., Woloszyn, K., Yang, C.F., Yoder, J.B., Rothschild, L. J., Wind, S.J., Hendrickson, W.A., Mao, C., Seeman, N.C., et al. (2023). Heterobimetallic Base Pair Programming in Designer 3D DNA Crystals. J. Am. Chem. Soc. *145*, 17945–17953. https://doi.org/10.1021/jacs.3c05478.
24. Tanaka, K., Tengeiji, A., Kato, T., Toyama, N., and Shionoya, M. (2003). A discrete self-assembled metal array in artificial DNA. Science *299*, 1212–1213.
25. Takezawa, Y., Mori, K., Huang, W.-E., Nishiyama, K., Xing, T., Nakama, T., and Shionoya, M. (2023). Metal-mediated DNA strand displacement and molecular device operations based on base-pair switching of 5-hydroxyuracil nucleobases. Nat. Commun. *14*, 4759.
26. Takezawa, Y., and Shionoya, M. (2012). Metal-mediated DNA base pairing: alternatives to hydrogen-bonded Watson–Crick base pairs. Acc. Chem. Res. *45*, 2066–2076.
27. Miyake, Y., Togashi, H., Tashiro, M., Yamaguchi, H., Oda, S., Kudo, M., Tanaka, Y., Kondo, Y., Sawa, R., Fujimoto, T., et al. (2006). MercuryII-mediated formation of thymine− HgII− thymine base pairs in DNA duplexes. J. Am. Chem. Soc. *128*, 2172–2173.
28. Ono, A., Cao, S., Togashi, H., Tashiro, M., Fujimoto, T., Machinami, T., Oda, S., Miyake, Y., Okamoto, I., and Tanaka, Y. (2008). Specific interactions between silver (I) ions and cytosine–cytosine pairs in DNA duplexes. Chem. Commun., 4825–4827.
29. Takezawa, Y., and Shionoya, M. (2023). Metal Ion-Induced changes in the Stability of DNA duplexes. In Handbook of Chemical Biology of Nucleic Acids (Springer), pp. 2645–2683.
30. Liu, B., Demir, B., Gultakti, C.A., Marrs, J., Gong, Y., Li, R., Oren, E.E., and Hihath, J. (2024). Self-Aligning Nanojunctions for Integrated Single-Molecule Circuits. ACS Nano *18*, 4972–4980.
31. Mengrani, Z., Hong, W., and Palma, M. (2024). DNA-Mediated Carbon Nanotubes Heterojunction Assembly. ACS Nanosci. Au *4*, 391–398.
32. Weizmann, Y., Chenoweth, D.M., and Swager, T.M. (2010). Addressable terminally linked DNA− CNT nanowires. J. Am. Chem. Soc. *132*, 14009–14011.
33. Feldman, A.K., Steigerwald, M.L., Guo, X., and Nuckolls, C. (2008). Molecular electronic devices based on single-walled carbon nanotube electrodes. Acc. Chem. Res. *41*, 1731–1741.
34. Huber, R., González, M.T., Wu, S., Langer, M., Grunder, S., Horhoiu, V., Mayor, M., Bryce, M.R., Wang, C., Jitchati, R., et al. (2008). Electrical conductance of conjugated oligomers at the single molecule level. J. Am. Chem. Soc. *130*, 1080–1084.
35. Alangari, M., Demir, B., Gultakti, C.A., Oren, E.E., and Hihath, J. (2023). Mapping DNA conformations using single-molecule conductance measurements. Biomolecules *13*, 129.
36. Xiang, L., Palma, J.L., Bruot, C., Mujica, V., Ratner, M.A., and Tao, N. (2015). Intermediate tunnelling–hopping regime in DNA charge transport. Nat. Chem. *7*, 221–226.
37. Conley, K., Mikladal, B., Gadgil, B., Etula, J., Juntunen, T., Varjos, I., and Karttunen, A.J. (2024). Dedoping of Carbon Nanotube Networks Containing Metallic Clusters and Chloride. J. Phys. Chem. C *128*, 18442–18450.
38. Reich, S., Thomsen, C., and Ordejón, P. (2002). Electronic band structure of isolated and bundled carbon nanotubes. Phys. Rev. B *65*, 155411.
39. Lu, B., Vecchioni, S., Ohayon, Y.P., Canary, J.W., and Sha, R. (2022). The wending rhombus: Self-assembling 3D DNA crystals. Biophys. J. *121*, 4759–4765.
40. Kim, S.H., Yi, S.-G., Park, M.U., Lee, C., Kim, M., and Yoo, K.-H. (2019). Multilevel MoS2 optical memory with photoresponsive top floating gates. ACS Appl. Mater. Interfaces *11*, 25306–25312.
41. Li, C., Fan, W., Lei, B., Zhang, D., Han, S., Tang, T., Liu, X., Liu, Z., Asano, S., Meyyappan, M., et al. (2004). Multilevel memory based on molecular devices. Appl. Phys. Lett. *84*, 1949–1951.
42. Zhang, X., Hu, H., Liu, W., Wang, Y., Liu, J., and Wu, P. (2021). Selective heavy atom effect forming photosensitizing hot spots in double-stranded DNA matrix. J. Phys. Chem. Lett. *12*, 9205–9212.
43. Müller, J., and Lippert, B. (2023). Modern Avenues in Metal-Nucleic Acid Chemistry (CRC Press)).
44. Wang, G.-L., Jin, L.-Y., Wu, X.-M., Dong, Y.-M., and Li, Z.-J. (2015). Label-free colorimetric sensor for mercury (II) and DNA on the basis of mercury (II) switched-on the oxidase-mimicking activity of silver nanoclusters. Anal. Chim. Acta *871*, 1–8.
45. Sinha, S., and Pal, T. (2022). A comprehensive review of FET-based pH sensors: materials, fabrication technologies, and modeling. Electrochem. Sci. Adv. *2*, e2100147.
46. Murke, S., Chen, W., Pezzotti, S., and Havenith, M. (2024). Tuning Acid–Base Chemistry at an Electrified Gold/Water Interface. J. Am. Chem. Soc. *146*, 12423–12430.

Please cite this article in press as: Liu et al., Electrical control of a metal-mediated DNA memory, Matter (2025), https://doi.org/10.1016/j.matt.2025.102470

47. Chen, Y., Wang, X., Erramilli, S., Mohanty, P., and Kalinowski, A. (2006). Silicon-based nanoelectronic field-effect pH sensor with local gate control. Appl. Phys. Lett. *89*, 223512.

48. Oldham, K.B. (2008). A Gouy–Chapman–Stern model of the double layer at a (metal)/(ionic liquid) interface. J. Electroanal. Chem. *613*, 131–138.

49. Doblhoff-Dier, K., and Koper, M.T.M. (2021). Modeling the Gouy–Chapman diffuse capacitance with attractive ion–surface interaction. J. Phys. Chem. C *125*, 16664–16673.

50. Chamberlayne, C.F., and Zare, R.N. (2020). Simple model for the electric field and spatial distribution of ions in a microdroplet. J. Chem. Phys. *152*, 184702.

51. Emsley, P., Lohkamp, B., Scott, W.G., and Cowtan, K. (2010). Features and development of Coot. Biological crystallography *66*, 486–501.

52. Case, D.A., Aktulga, H.M., Belfon, K., Ben-Shalom, I.Y., Berryman, J.T., Brozell, S.R., Cerutti, D.S., Cheatham III, T.E., Cisneros, G.A., and Cruzeiro, V.W.D. (2023). Amber 2023 (University of California).

53. Vecchioni, S., Lu, B., Livernois, W., Ohayon, Y.P., Yoder, J.B., Yang, C.F., Woloszyn, K., Bernfeld, W., Anantram, M.P., Canary, J.W., et al. (2023). Metal-Mediated DNA Nanotechnology in 3D: Structural Library by Templated Diffraction. Adv. Mater. *35*, e2210938. https://doi.org/10.1002/adma.202210938.

54. Frisch, M.J., Trucks, G.W., Schlegel, H., Scuseria, G.E., Robb, M.A., Cheeseman, J.R., Scalmani, G., Barone, V., Petersson, G.A., and Nakatsuji, H. (2023). Gaussian 16, Revision C. 01. Gaussian, Inc., Wallingford CT..

55. Chapman, D.L. (1913). LI. A contribution to the theory of electrocapillarity. London, Edinburgh Dublin Phil. Mag. J. Sci. *25*, 475–481.

56. Lee, C.-C., Lee, H., Hyon, Y., Lin, T.-C., and Liu, C. (2010). New Poisson–Boltzmann type equations: one-dimensional solutions. Nonlinearity *24*, 431–458.

57. Lu, B., Zhou, Y., Holst, M., and McCammon, J. (2008). Recent progress in numerical methods for the Poisson-Boltzmann equation in biophysical applications. Commun. Comput. Phys. *3*, 973–1009.

Matter, Volume *9*

Supplemental information

Electrical control of a metal-mediated DNA memory

Bo Liu, Brandon Lu, Arpan De, Kyoungdu Kim, Lara Perren, Karol Woloszyn, Galina Petrova, Ruihao Li, Chu-fan Yang, Chengde Mao, Antia S. Botana, Yoel P. Ohayon, James W. Canary, Ruojie Sha, M.P. Anantram, Simon Vecchioni, and Joshua Hihath

Supplemental Information

Electrical Control of a Metal-Mediated DNA Memory

Bo Liu,[1,6] Brandon Lu,[2,6] Arpan De,[3] Kyoungdu Kim,[1] Lara Perren,[2] Karol Woloszyn,[2] Galina Petrova,[3] Ruihao Li,[1] Chu-fan Yang,[2] Chengde Mao,[4] Antia S. Botana,[5] Yoel P. Ohayon,[2] James W. Canary,[2] Ruojie Sha,[2] M.P. Anantram,[3,*] Simon Vecchioni,[2,**] Joshua Hihath[1,7,***]

[1]Center for Bioelectronics and Biosensors, School of Electrical, Computer, and Energy Engineering, Arizona State University, Tempe, Arizona 85287, USA

[2]Department of Chemistry, New York University, New York, NY 10003, USA

[3]Department of Electrical and Computer Engineering, University of Washington, Seattle, WA 98195, USA

[4]Department of Chemistry, Purdue University, West Lafayette, IN 47907, USA

[5]Department of Physics, Arizona State University, Tempe, Arizona 85281, USA

[6]These authors contributed equally

[7]Lead contact

*Corresponding authors: M.P.A.(anant@uw.edu)

**Corresponding authors: S.V. (sv1091@nyu.edu)

***Corresponding authors: J.H. (jhihath@asu.edu)

The PDF file includes:

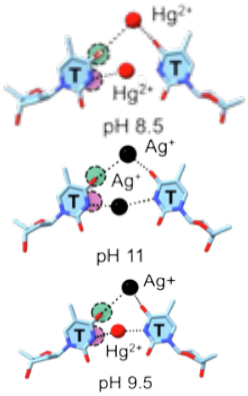
Materials and Methods
Tables S1 to S7
Figures S1 to S10

Supplemental Methods

Materials:

The sequence for metal mediated DNA(mmDNA)

5'-amino-$(CH_2)_6$-GCCATACAC-$(CH_2)_6$-amino-3'
$[Hg^{2+}]_2$
GTGTTTGGC



5'-amino-$(CH_2)_6$-GCCATACAC-$(CH_2)_6$-amino-3'
$[Ag^+]_2$
GTGTTTGGC

5'-amino-$(CH_2)_6$-GCCATACAC-$(CH_2)_6$-amino-3'
$[Ag^+][Hg^{2+}]$
GTGTTTGGC

5'-amino-$(CH_2)_6$-GCCATACAC-$(CH_2)_6$-amino-3' (Control Experiments)
GTGTATGGC

ssDNA mCNT wrapping sequence:

5'-(GT)20-3'

Buffer Solutions:

pH =11	25 μM $HgCl_2$	25 μM $AgNO_3$	125 mM $MgSO_4$	380.0 μM NaOH	40mM Tris
pH =9.5	25 μM $HgCl_2$	25 μM $AgNO_3$	125 mM $MgSO_4$	32.0 μM NaOH	40mM Tris
pH =8	25 μM $HgCl_2$	25 μM $AgNO_3$	125 mM $MgSO_4$	1.0 μM NaOH	40mM Tris

These buffers were used for all pH dependent experiments, for the gating experiments, the Tris was omitted to allow maximum control over the local pH.

Metallic single wall carbon nanotubes (mCNTs)

Metallic single wall carbon nanotubes (mCNTs) were purchased from Nano Integris, Inc.

Chemicals

Dulbecco's phosphate buffered saline (DPBS), Hexafluorophosphate azabenzotriazole tetramethyl uronium (HATU), Ethylenediaminetetraacetic acid (EDTA) were purchased from Thermo Fisher Scientific. All other analytical-grade chemicals were purchased from Sigma Aldrich.

XRD (X-ray Diffraction)

Oligo Name	Sequence	Type
7W1	/5Phos/CTGATGTGGCTGCT	Crossover strand (strand 1)
7T2	GAGCAGCCTGTTTGGACATCA	Helical strand (strand 2)
7T3	TACACCATACACCATACACCA	Center strand (strand 3)
T1	GTGTTTGGC	Transistor sequence 1
T2amm	[C6amino]-GCCATACAC-[C6amino]	Transistor sequence 2
A1	GTGTATGGC	Control sequence 1

Table S1. Oligonucleotide sequences used in this study

Buffer composition for crystal growth was based on prior work. All crystals were grown in 40 mM Tris, 125 mM $MgSO_4$, at pH values of 8.0, 9.5, and 11.0, equilibrated using NaOH. Crystals were grown in 10 µL hanging drops by vapor diffusion in a thermally controlled incubator. Drops contained 60 pmol, 6 µM, of each triangle motif (18 µM helical and crossover strands, 6 µM center strand). Metal counterions were added in twofold excess to binding sites, corresponding to 36 µM $AgNO_3$ and 36 µM $HgCl_2$. Hanging drops were equilibrated against a reservoir containing a tenfold increase in concentration: 400 mM Tris and 1.25 M $MgSO_4$, and the desired pH value. Crystals were heated to 65 °C at 5 °C/hour, and cooled down to 20 °C at a rate of 0.4 °C/hour. Crystals were then transferred to cryoprotectant solution containing 70% of the buffer solution of the crystal reservoir and 30% glycerol re-adjusted to the appropriate pH. Cryoprotectant contained either [2:2:1], a [4:2:1] or a [0:2:1] ratio of [Hg^{2+}:Ag^{+}:T-T pairs], as delineated in **Table S2**. Crystals were frozen after specified time points by immersion in liquid nitrogen to halt transmetalation. Crystals were then shipped for X-ray diffraction.

Time (s)	Resolution (Å)	N3 Ion	N3 Occupancy	N3 f'' Value	O4 Ion	O4 Occupancy	O4 f'' Value
pH 8.0→9.5, 2[Ag+] in T:T base pair							
4	5.21	Hg	1.00	11.15	N/A	N/A	N/A
16	4.82	Hg	0.85	10.20	N/A	N/A	N/A
35	3.94	Hg	0.61	11.13	Hg	0.18	9.62
75	5.46	Hg	0.77	10.94	Hg	0.22	10.36
pH 8.0→9.5, 2[Hg2+] 2[Ag+] in T:T base pair							
50	5.21	Hg	1.00	11.15	N/A	N/A	N/A
97	4.82	Hg	0.85	10.20	N/A	N/A	N/A
pH 9.5→11.0, 2[Ag+] in T:T base pair							
50	5.21	Hg	1.00	11.15	N/A	N/A	N/A
97	4.82	Hg	0.85	10.20	N/A	N/A	N/A
pH 9.5→11.0, 2[Hg2+] 2[Ag+] in T:T base pair							
7	5.21	Hg	1.00	11.15	N/A	N/A	N/A
21	4.82	Hg	0.85	10.20	N/A	N/A	N/A
pH 11.0→9.5, 2[Hg2+] 2[Ag+] in T:T base pair							
5	5.21	Hg	1.00	11.15	N/A	N/A	N/A
pH 8.0→9.5, 2[Hg2+] 2[Ag+] in T:T base pair							
4	5.21	Hg	1.00	11.15	N/A	N/A	N/A
7	4.82	Hg	0.85	10.20	N/A	N/A	N/A
11	5.46	Hg	0.77	10.94	Hg	0.22	10.36
pH 8.5→11.0, 4[Hg^{2+}] 2[Ag^{+}] in T:T base pair							
30	6.61	N/A	N/A	N/A	N/A	N/A	N/A
60	5.36	N/A	N/A	N/A	Hg	0.22	7.41
90	5.19	N/A	N/A	N/A	Hg	0.20	5.46
300	5.25	N/A	N/A	N/A	Ag	1.00	4.27
pH 11.0→7.0, 4[Hg^{2+}] 2[Ag^{+}] in T:T base pair							
5	5.21	Hg	1.00	11.15	N/A	N/A	N/A
30	4.82	Hg	0.85	10.20	N/A	N/A	N/A
60	3.94	Hg	0.61	11.13	Hg	0.18	9.62
90	5.46	Hg	0.77	10.94	Hg	0.22	10.36
300	4.69	Hg	0.65	10.49	Hg	0.39	10.95

Table S2. Time spent in pH1(value in red) cryoprotectant solution. Resolution of crystal structures, N3 and O4 position ion identity with refined f'' values are listed for dT:Ag^{+}/Hg^{2+}:dT crystals originally grown from pH2 (value in black).

Data Collection

X-ray diffraction data were collected at beamlines 17-ID-1, 17-ID-2, and 19-ID at the National Synchrotron Light Source II (NSLS-II) at Brookhaven National Laboratory and beamline 17-ID at the Advanced Photon Source (APS) at Argonne National Laboratory. Data were processed using the autoPROC webserver and scaled using STARANISO. Resolution cutoffs were based on local I/σ value of 1.2 with an "ellipsoidal," non-spherical cutoff. Structures were solved by molecular replacement with model 7SM2 and anomalous scattering techniques using Phenix AutoSol (MR-SAD). Structures and Heavy atom identification were refined using Phenix refine and COOT. Structures were deposited under accession ID's listed in Tables **S3-S7**.

Diffraction Tables:

[·]Values in parentheses for highest resolution shell

[a]Data scaling performed with ellipsoidal cutoff using the STARANISO server (Global Phasing), with severe anisotropy observed in all crystals along the three-fold axis.

Reconfiguration	8.0 → 9.5	8.0 → 9.5	8.0 → 9.5	8.0 → 9.5
Time soaked	4 seconds	16 seconds	35 seconds	75 seconds
[Hg^{2+}:Ag^{+}:TT]	[0:2:1]	[0:2:1]	[0:2:1]	[0:2:1]
Data collection	PDB (**9MM7**)	PDB (**7MM8**)	PDB (**9MM9**)	PDB (**9ND7**)
Wavelength (Å)	0.97856	0.97856	0.97856	0.97856
Space Group	R3	R3	R3	R3
Cell dimensions				
a = *b* = *c* (Å)	68.35	68.21	68.01	67.77
α = β = γ (°)	100.11	100.20	100.71	100.80
Resolution (Å)	19.80-4.88 (5.60-4.88)	42.06-4.61 (5.18-4.61)	19.80-4.50 (4.93-4.39)	19.74-5.70 (6.50-5.70)
I / σI	5.7 (1.4)	7.5 (1.1)	8.0 (0.6)	6.0 (0.7)
$CC_{1/2}$	0.993 (0.676)	0.993 (0.662)	0.994 (0.439)	0.991 (0.313)
Completeness ellipsoidal (%)	84.5 (48.7)	86.5 (55.8)	85.8 (50.9)	86.6 (56.2)
Redundancy	5.6 (5.5)	11.3 (10.1)	5.5 (4.9)	5.5 (5.7)
Refinement				
Resolution (Å)	19.80-4.88	42.06-4.61	19.80-4.50	19.74-5.70
No. reflections	2657	3132	3426	1794
R_{work} / R_{free}	0.170/0.209	0.204/0.226	0.217/0.265	0.140/0.224
No. atoms	860	860	860	860
DNA	858	858	858	858
Ligand/ion	2	2	2	2
Water	0	0	0	0
B-factors	331	236	313	243
DNA	331	236	313	243
Ligand/ion	182	156	192	109
R.m.s deviations				
Bond lengths (Å)	0.0165	0.0093	0.0078	0.0211
Bond angles (°)	1.584	1.175	1.026	1.912

Table S3. Data collection, phasing, and refinement statistics for dT:Ag^{+}/Hg^{2+}:dT structures.

Reconfiguration	8.0 → 9.5	8.0 → 9.5	11.0 → 9.5	9.5 → 11.0	9.5 → 11.0
Time soaked	50 seconds	97 seconds	5 seconds	20 seconds	40 seconds
[Hg^{2+}:Ag^{+}:TT]	[2:2:1]	[2:2:1]	[2:2:1]	[0:2:1]	[0:2:1]
Data collection	PDB (**9ND6**)	PDB (**9ND8**)	PDB (**9ND9**)	PDB (**9MMA**)	PDB (**9MMB**)
Wavelength (Å)	0.97856	0.97856	0.97856	0.97856	0.97856
Space Group	R3	R3	R3	R3	R3
Cell dimensions					
a = *b* = *c* (Å)	68.08	67.93	68.48	68.11	68.20
α = β = γ (°)	101.01	105.15	100.03	100.06	99.98
Resolution (Å)	19.86-4.89 (5.52-4.89)	19.91- 5.38 (6.17-5.38)	19.83-4.65 (5.19-4.65)	19.73-5.03 (5.61-5.03)	19.75-4.72 (5.16-4.60)
I / σI	7.6 (1.3)	5.9 (1.0)	7.7 (1.1)	6.9 (1.2)	8.6 (0.9)
$CC_{1/2}$	0.995 (0.477)	0.994 (0.320)	0.996 (0.614)	0.996 (0.418)	0.998 (0.382)
Completeness ellipsoidal (%)	86.1 (52.6)	85.9 (55.9)	86.2 (50.9)	86.6 (53.3)	86.9 (52.6)
Redundancy	5.5 (5.3)	5.5 (5.7)	5.5 (5.0)	5.5 (5.4)	5.6 (4.8)
Refinement					
Resolution (Å)	19.86-4.89	19.91-5.38	19.83-4.66	19.73-5.03	19.75-4.72
No. reflections	2705	2072	2996	2587	3112
R_{work} / R_{free}	0.157/0.172	0.169/0.245	0.165/0.180	0.179/0.194	0.148/0.165
No. atoms	860	860	860	860	860
DNA	858	858	858	858	858
Ligand/ion	2	2	2	2	2
Water	0	0	0	0	0
B-factors	347	371	342	313	288
DNA	347	371	342	313	288
Ligand/ion	131	138	134	151	154
R.m.s deviations					
Bond lengths (Å)	0.0159	0.0010	0.0088	0.0084	0.0171
Bond angles (°)	1.571	1.229	1.1193	1.137	1.669

Table S4. Data collection, phasing and refinement statistics for dT:Ag^{+}/Hg^{2+}:dT structures.

Reconfiguration	9.5→ 11.0	9.5→ 11.0	9.5→ 8.0	9.5→ 8.0
Time soaked	7 seconds	21 seconds	4 seconds	7 seconds
[Hg^{2+}:Ag^{+}:TT]	[2:2:1]	[2:2:1]	[2:2:1]	[2:2:1]
Data collection	PDB (**9MMC**)	PDB (**9MMD**)	PDB (**9MM3**)	PDB (**9MM4**)
Wavelength (Å)	0.97856	0.97856	1.007428	1.007428
Space Group	R3	R3	R3	R3
Cell dimensions				
a = *b* = *c* (Å)	68.38	68.74	68.13	68.64
α = β = γ (°)	100.81	100.46	100.74	100.12
Resolution (Å)	19.92-4.70 (5.31-4.70)	19.97-5.03 (5.76-5.03)	19.83-6.43 (9.02-6.43)	41.15-6.50 (8.07-6.50)
I / σI	8.5 (0.9)	5.6 (1.2)	3.1 (1.1)	3.2 (0.9)
$CC_{1/2}$	0.998 (0.514)	0.993 (0.139)	0.975 (0.895)	0.999 (0.392)
Completeness ellipsoidal (%)	86.1 (56.8)	84.1 (48.9)	80.9 (57.2)	64.3 (48.1)
Redundancy	5.6 (5.0)	5.4 (5.5)	3.6 (4.1)	2.2 (2.1)
Refinement				
Resolution (Å)	19.92-4.70	19.97-5.03	19.83-6.43	41.15-6.50
No. reflections	2786	2556	932	836
R_{work} / R_{free}	0.154/0.1598	0.198/0.206	0.197/0.280	0.152/0.82
No. atoms	860	860	860	860
DNA	858	858	858	858
Ligand/ion	2	2	2	2
Water	0	0	0	0
B-factors	327	239	186	473
DNA	327	239	186	473
Ligand/ion	149	123	160	153
R.m.s deviations				
Bond lengths (Å)	0.0093	0.0078	0.0066	0.0073
Bond angles (°)	1.152	1.023	0.938	0.984

Table S5. Data collection, phasing and refinement statistics for dT:Ag^{+}/Hg^{2+}:dT structures grown at pH 9.5.

Reconfiguration	11.0→ 7.0	11.0→ 7.0	11.0→ 7.0	11.0→ 7.0	11.0→ 7.0
Time soaked	5 seconds	30 seconds	60 seconds	90 seconds	5 minutes
[Hg^{2+}:Ag^{+}:TT]	[4:2:1]	[4:2:1]	[4:2:1]	[4:2:1]	[4:2:1]
Data collection	PDB (**7TG4**)	PDB (**7TG6**)	PDB (**7TG7**)	PDB (**7TG8**)	PDB (**7TG9**)
Wavelength (Å)	1.00743	1.00743	1.00743	1.00743	1.00743
Space Group	R3	R3	R3	R3	R3
Cell dimensions					
$a = b = c$ (Å)	68.93	68.54	68.70	68.41	67.98
$\alpha = \beta = \gamma$ (°)	102.11	102.48	100.91	103.08	102.22
Resolution (Å)	64.97-5.21 (6.06-5.21)	64.33-4.82 (5.45-4.82)	65.59-3.94 (4.29-3.94)	63.72-5.46 (6.21-5.46)	64.00-4.69 (5.35-4.69)
Ellipsoidal diffraction limits (Å)[a]	5.12, 5.12, 5.96	4.66, 4.66, 5.68	3.86, 3.86, 4.78	5.23, 5.23, 5.86	4.52, 4.52, 6.16
R_{merge}	0.171 (2.70)	0.124 (2.14)	0.086 (3.21)	0.156 (3.17)	0.104 (1.74)
$I / \sigma I$	6.9 (1.1)	8.9 (1.1)	9.8 (0.7)	7.8 (0.8)	9.7 (1.4)
$CC_{1/2}$	0.998 (0.255)	0.998 (0.473)	0.991 (0.192)	0.995 (0.305)	0.998 (0.576)
Completeness ellipsoidal (%)	84.4 (50.5)	86.7 (58.2)	87.9 (52.2)	87.0 (58.0)	85.1 (59.0)
Redundancy	10.3 (10.8)	10.2 (11.0)	10.0 (9.6)	10.6 (11.3)	10.1 (10.9)
Refinement					
Resolution (Å)	32.74-5.21	32.59-4.82	32.79-3.94 (4.96-3.94)	32.56-5.46	32.30-4.69
No. reflections	2213	2661	4970 (1464)	2091	2462
R_{work} / R_{free}	0.265/0.328	0.195/0.275	0.203/0.235 (0.354/0.351)	0.251/0.292	0.165/0.170
No. atoms	859	859	860	860	860
DNA	858	858	858	858	858
Ligand/ion	1	1	2	2	2
Water	0	0	0	0	0
B-factors	285	280	256	319	264
DNA	285	280	256	319	264
Ligand/ion	110	157	143	199	102
R.m.s deviations					
Bond lengths (Å)	0.0068	0.0087	0.0079	0.0067	0.0162
Bond angles (°)	0.995	1.123	1.076	0.975	1.561

Table S6. Data collection, phasing and refinement statistics for dT:Ag^{+}/Hg^{2+}:dT structures grown at pH 11.0 and soaked in pH 7.0 with metals in the cryoprotectant solution.

Space Group	R3	R3	R3	R3
Cell dimensions				
$a = b = c$ (Å)	67.98	68.36	68.49	68.23
$\alpha = \beta = \gamma$ (°)	105.56	101.53	102.66	102.85
Resolution (Å)	60.93-6.61 (9.18-6.61)	64.86-5.36 (6.17-5.36)	64.14-5.19 (5.86-5.19)	63.74-5.25 (6.11-5.25)
Ellipsoidal diffraction limits (Å)[a]	6.04, 6.04, 6.31	5.12, 5.12, 6.04	4.96, 4.96, 5.76	4.96, 4.96, 6.64
R_{merge}	0.556 (1.81)	0.092 (2.26)	0.126 (2.64)	0.158 (2.24)
$I / \sigma I$	5.1 (2.1)	8.0 (0.8)	9.4 (0.9)	7.6 (1.1)
$CC_{1/2}$	0.988 (0.765)	0.996 (0.531)	0.996 (0.226)	0.994 (0.365)
Completeness ellipsoidal (%)	82.9 (72.3)	86.0 (58.3)	87.1 (57.5)	86.1 (66.9)
Redundancy	7.5 (7.6)	9.9 (10.9)	10.5 (11.0)	10.5 (10.9)
Refinement				
Resolution (Å)	60.93-6.61	41.02-5.36	32.57-5.19	63.74-5.25
No. reflections	466	2140	2397	2009
R_{work} / R_{free}	0.357/0.424	0.163/0.195	0.251/0.309	0.238/0.269
No. atoms	858	860	860	860
DNA	858	858	858	858
Ligand/ion	0	2	2	2
Water	0	0	0	0
B-factors	516	398	468	316
DNA	516	398	468	316
Ligand/ion	N/A	132	103	94
R.m.s deviations				
Bond lengths (Å)	0.0063	0.0142	0.0069	0.0100
Bond angles (°)	0.9099	1.443	0.969	1.162

Table S7. Data collection, phasing and refinement statistics for dT:Ag^{+}/Hg^{2+}:dT structures grown at pH 8.5 and soaked in pH 11.0 with metals in the cryoprotectant solution.

Supporting Figures:

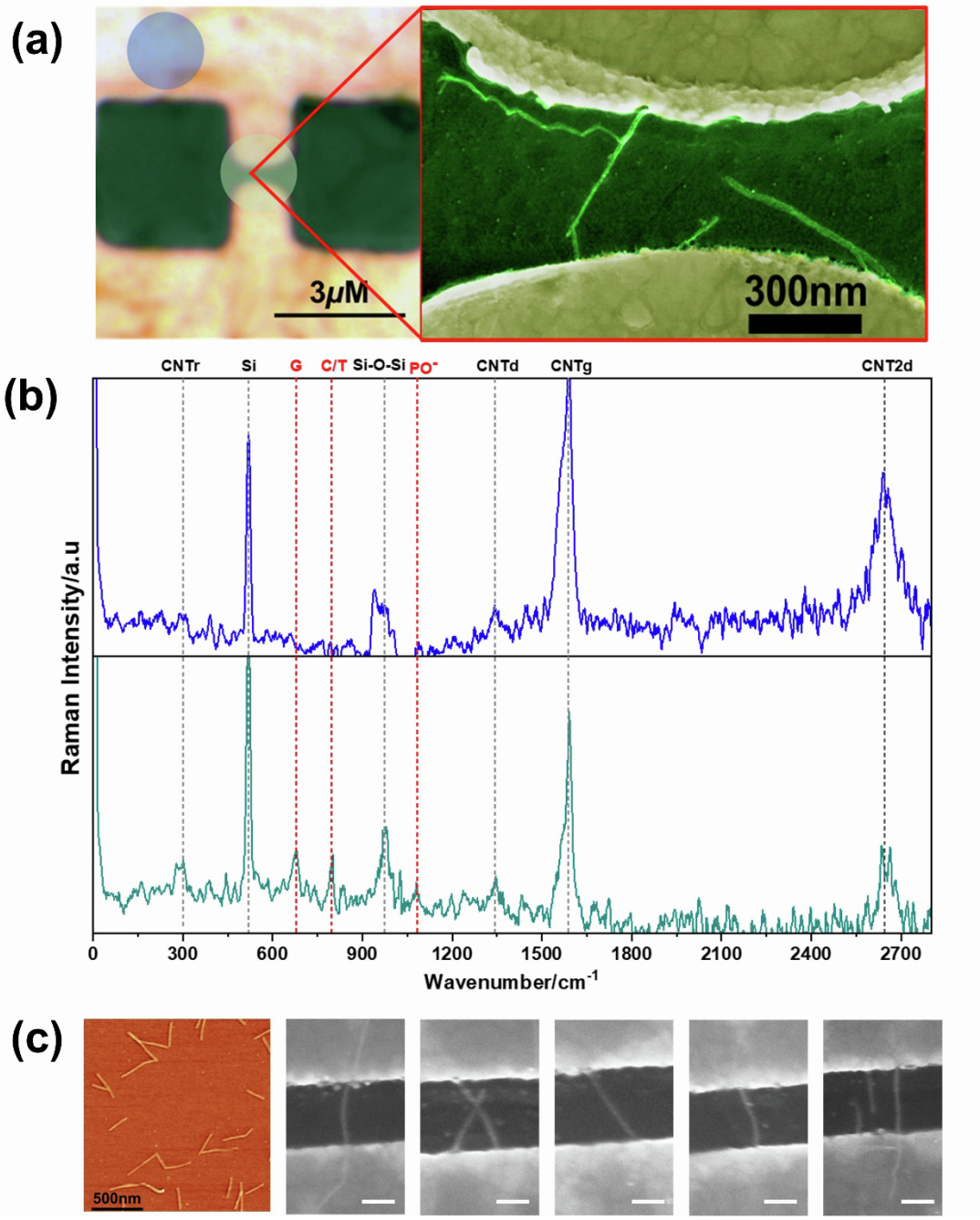


Figure S1. **Characterization of mCNT-mmDNA-mCNT devices. (a)** SEM image (Right image) of one of the devices showing a single mCNT-mmDNA-mCNT bridge between the electrodes. We performed Raman spectroscopy on different regions on the chip as indicated in the SEM. Left image highlights green area is electrode gap where we find the mCNT-mmDNA-mCNT junction. **(b)** Raman spectroscopy revealed signals of nanotubes in the gap region (green) and in areas away from the gap region (blue), DNA-related peak signals also appeared in the green highlighted region. **(c)** AFM and SEM characterization of mCNT-mmDNA-mCNT junctions. In the AFM image (left image, on mica substrate) angled discontinuities are often observed, indicating the successful bridging of a DNA duplex between two metallic carbon nanotubes. SEM images of additional devices, showing variations in junction alignment and morphology across different electrode pairs; each image captures a bridged device within the ~300 nm gap (scale bar=150 nm).

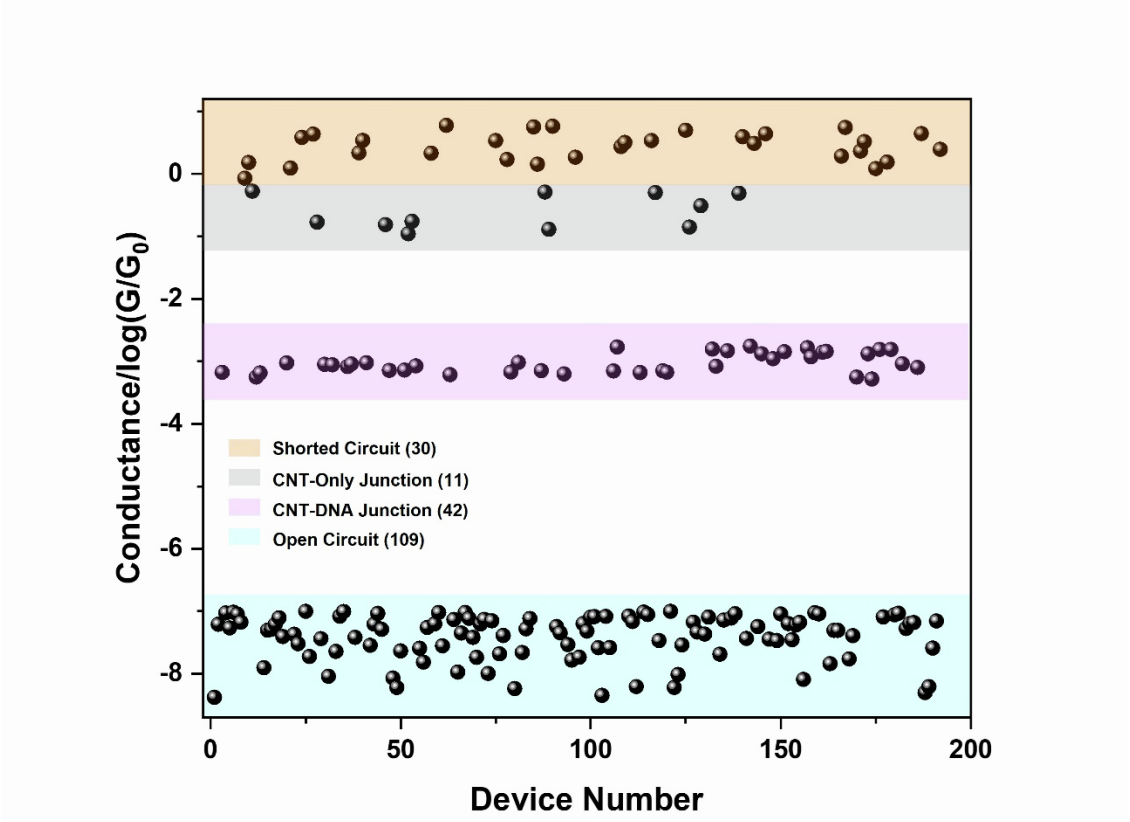


Figure S2. Statistical data of electrical measurements across 6 chips (192 electrode pairs total). Orange region indicates short circuits caused by fabrication defects (e.g., lithography misalignment or metal residue, ~15% occurrence), light gray region is high conductance devices suggesting direct CNT bridging across the electrodes (~6%), pink region is CNT-DNA junctions (pH switchable conductance, ~22% yield), and the blue region is blank electrodes (negligible pA currents, ~57%). The short circuits are primarily due to manufacturing imperfections, CNT-only cases arise from incomplete DNA hybridization or excess CNTs not removed by rinsing/centrifugation, and blanks reflect gaps without bridging.

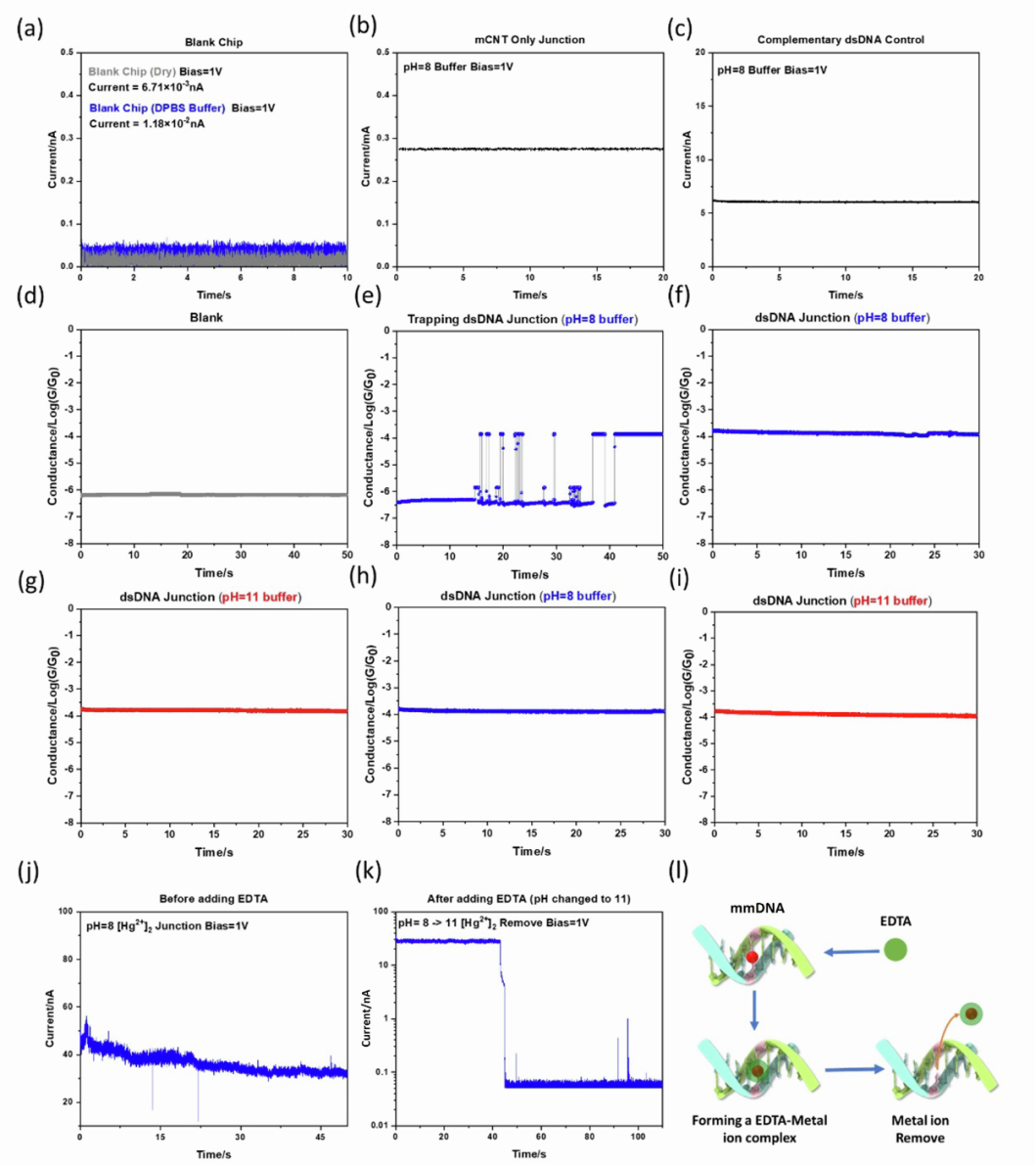


Figure S3. On-chip control experiments for mmDNA-based devices. (a) Current vs. time (I-t) trace for a blank chip in both wet (DPBS buffer) and dry conditions **(b)** I-t Trace of mCNT only junction, control experiments with mCNT-only junctions and blank chips confirm that observed conductance arises from single DNA-bridged devices. **(c)** I-t trace of the matched DNA sequence as control experiment. **(d,e)** To investigate the buffer's influence on complementary dsDNA, a dsDNA junction devoid of metal ions was added into a pH 8 buffer. A mCNT-dsDNA-mCNT junction was subsequently captured and immobilized between electrodes within 10 minutes. The observed conductance spikes indicate several temporary binding events before stabilizing. **(f-i)** Once the junction is stabilized between the electrodes, the buffer solution was carefully exchanged in a sequential manner, transitioning from pH 8 to 11, then back to 8, and finally to 11. There are no significant changes in the conductance of junction. **(j-l)** To verify the role of the metal ion and to explore the possibility of a sequence without metal but with the T:T base pair, EDTA (Ethylenediaminetetraacetic acid) was employed to extract metal ions from the metal mediated DNA (mmDNA) sequence. Initial current measurements were taken prior to EDTA addition. Approximately 40 seconds after introducing EDTA to the solution, a pronounced decrease in current is observed, accompanied by brief transitional states. EDTA ion, as a strong chelating agent, forms stable complexes with Hg^{2+} ions, effectively extracting these metal ions from the mmDNA structure.

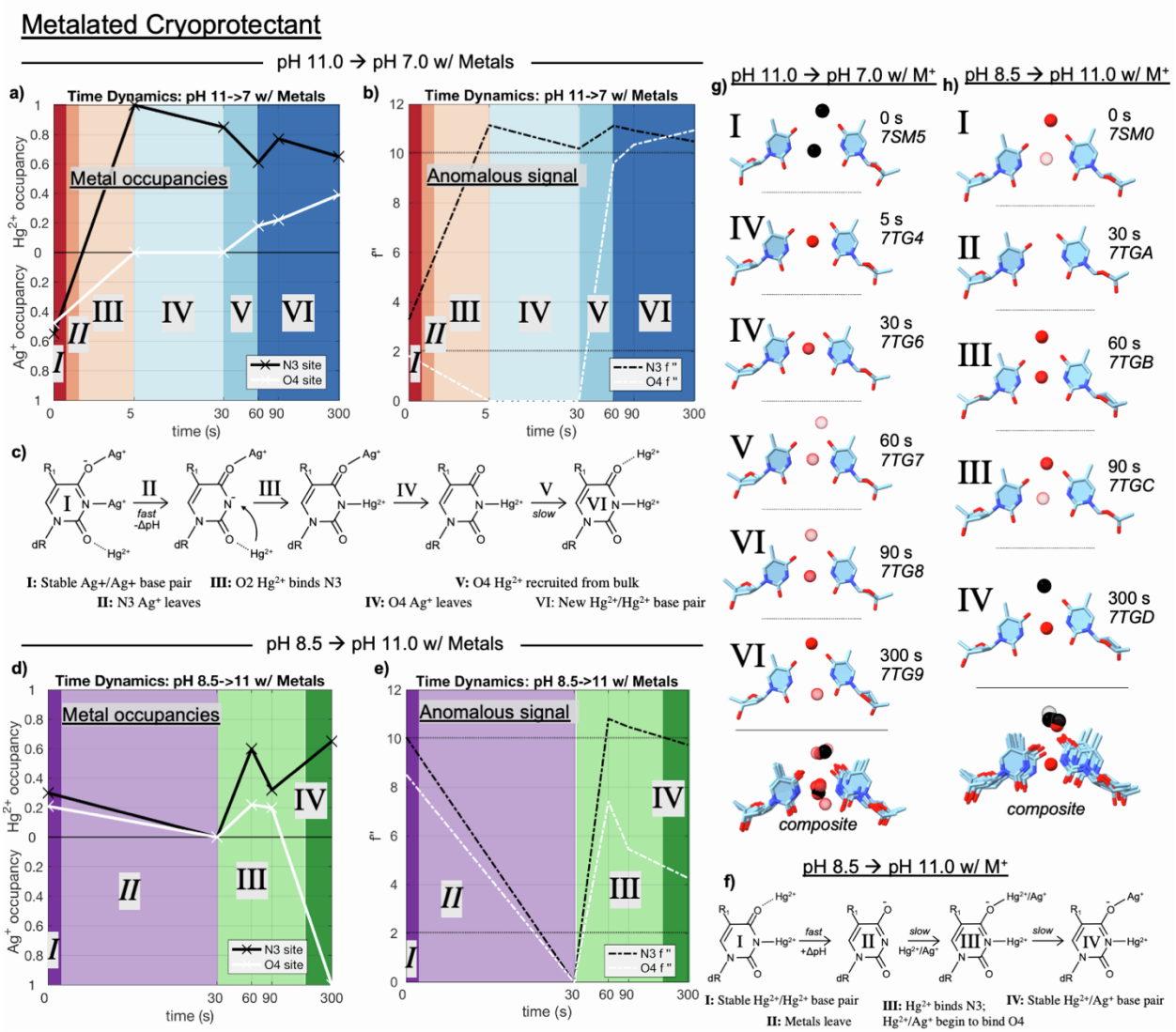


Figure S4. Time-resolved crystallography of transmetalation reaction in dT:Hg^{2+}/Hg^{2+}:dT as pH changed from 11.0 to 7.0, and from 8.5 to 11.0 in metalated cryoprotectant with a [4:2] ratio of [Hg^{2+}:Ag^{+}]. (a) Occupancies of Hg^{2+} on the positive y axis and Ag^{+} on negative y axis at the N3 and O4 sites are plotted over log-scaled time after the pH is changed from 11.0 to 7.0. **(b)** These data complement f″ anomalous plots of each site over log time. Horizontal dotted lines included to show calculated Hg^{2+} and Ag^{+} f″ at 12307 eV (10.17 and 2.06, respectively). This reaction shows a competition between Ag^{+} and Hg^{2+} for the O4 site, as well as an N3-bound Hg^{2+}. **(c)** When structures capture the reverse reaction from pH 8.5 to 11.0, the reaction is observed in reverse, with the important exception of a captured N3 Hg^{2+}, which is bound sometime after the fast rearrangement at 5s. **(e-g)** Crystal structure shown at each time point, with transparency of ions (Hg^{2+}: red spheres; Ag^{+}: black spheres) set to the normalized occupancy for each site. These data indicate that metal concentration needed to be tuned to yield a fully-reversible reaction. Furthermore, bulk concentration in the crystal yields resistance to N3 Hg^{2+} loss, which ultimately necessitated the half-steps, from 8.0 to 9.5, and 9.5 to 11.0, that are observed in **Fig 3**.

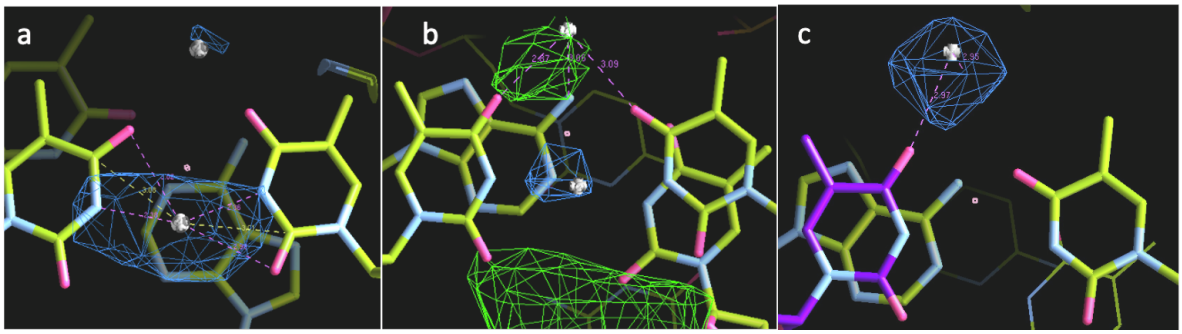


Figure S5. Electron density maps for lower resolution data visualized in COOT. At 4.69 Å, two density centers were observed (Figure S4a). Below 5 Å, $2F_o$-F_c maps struggled to resolve multiple sites between pyrimidines. Thus, F_o-F_c maps were used with $2F_o$-F_c for initial refinement (Figure S4b). Multiple sites were confirmed below 5 Å with correct f'' values. **(a)** dT: Ag^+/Hg^{2+}:dT pH 11.0 soaked for 5 mins in pH 7.0 cryoprotectant solution containing metals at 4.69 Å $2F_o$-F_c map contoured at 6.5 rmsd with both N3 and O4 sites visible (blue). **(b)** dT: Ag^+/Hg^{2+}:dT pH 11.0 soaked for 90 s in pH 7 cryoprotectant solution containing metals at 5.46 Å $2F_o$-F_c map contoured at 5.8 rmsd with only the N3 site visible (blue) and F_o-F_c difference map contoured at 3.0 rmsd showing density at the O4 site (green). The F_o-F_c map effectively acts as an omit map to determine the presence of the additional O4 site. O4 Hg^{2+} ion has an occupancy of 0.22 and f'' value of 10.36 which, combined with the F_o-F_c density, unequivocally confirms the presence of the second Hg^{2+} ion. **(c)** dT: Ag^+/Hg^{2+}:dT pH 8.5 soaked for 30s in pH 11.0 cryoprotectant solution at 5.94 Å. $2F_o$-F_c map contoured at 6.02 rmsd around 0.38 occupancy Ag^+ with a refined f'' value of 2.34 unequivocally shows the presence of an O4 Ag^+ metal.

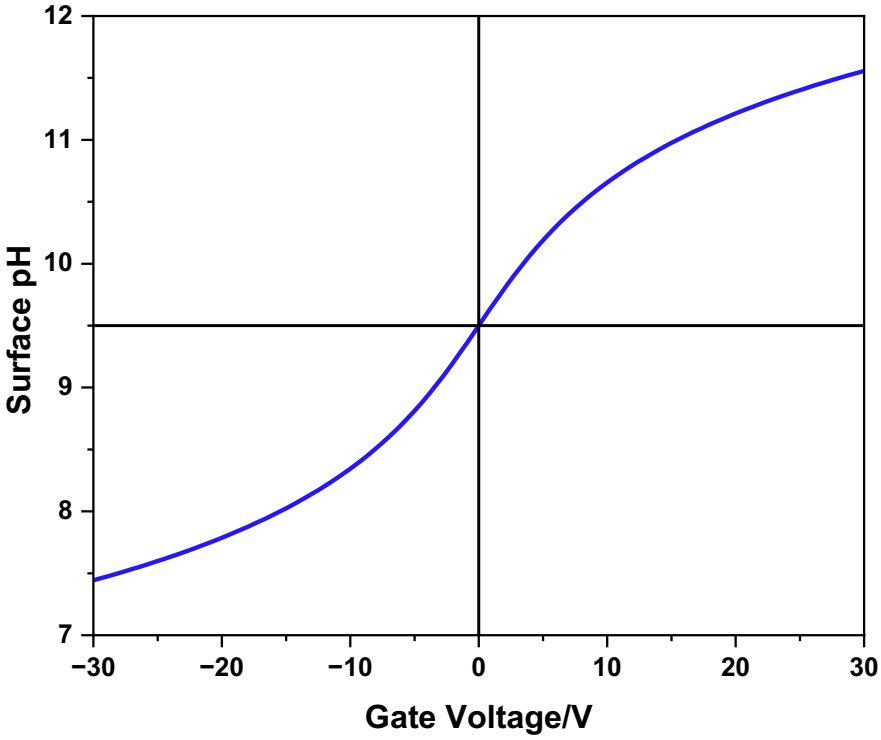
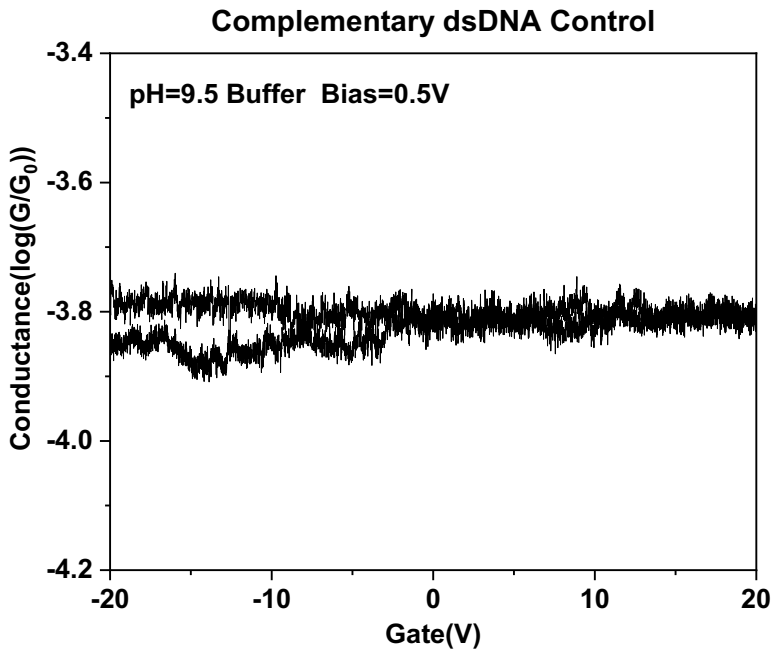
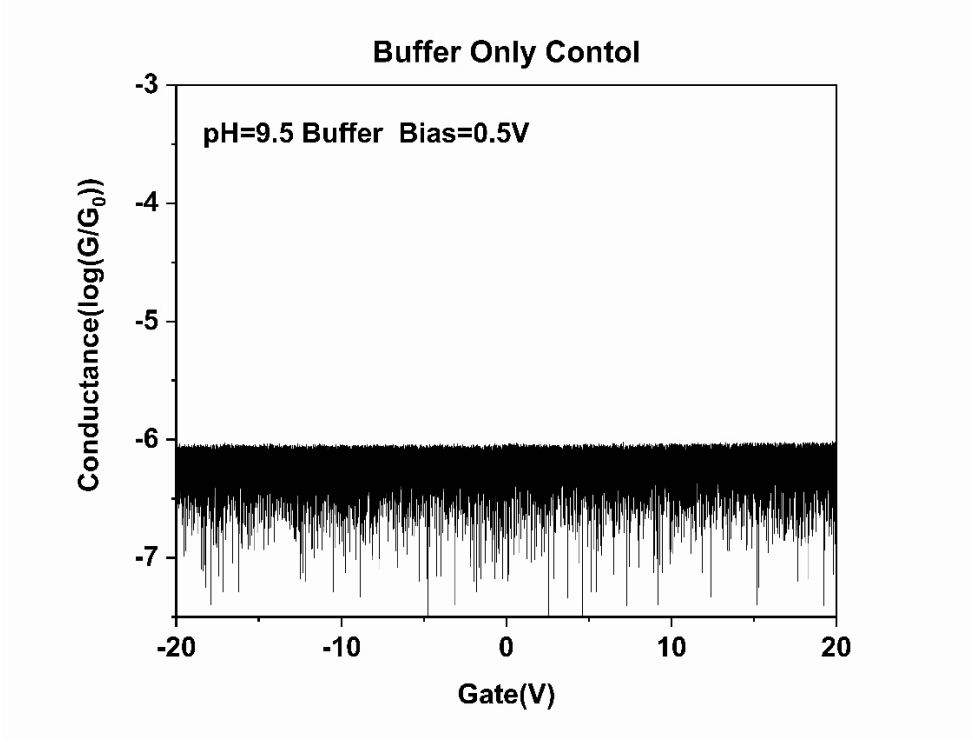


Figure S6. Estimation of the relationship between local pH and applied gate voltage. Based on the GCS model, estimated gate voltages of ±30 V correspond to local pH values of approximately 11 and 7.5, respectively. These calculated pH values closely match the experimentally observed pH switching behavior.

299 **(a)**



300 **(b)**



301
302
303 **Figure S7. Gate control experiment on complementary DNA at pH=9.5 and buffer-only solution. (a)**
304 Conductance vs. gate response (V_{scan} = 0.05 V/s) of a complimentary DNA at a bulk pH=9.5 as the control.
305 **(b)** Typical conductance vs. gate response (V_{scan} = 0.05 V/s) of buffer only control.
306
307

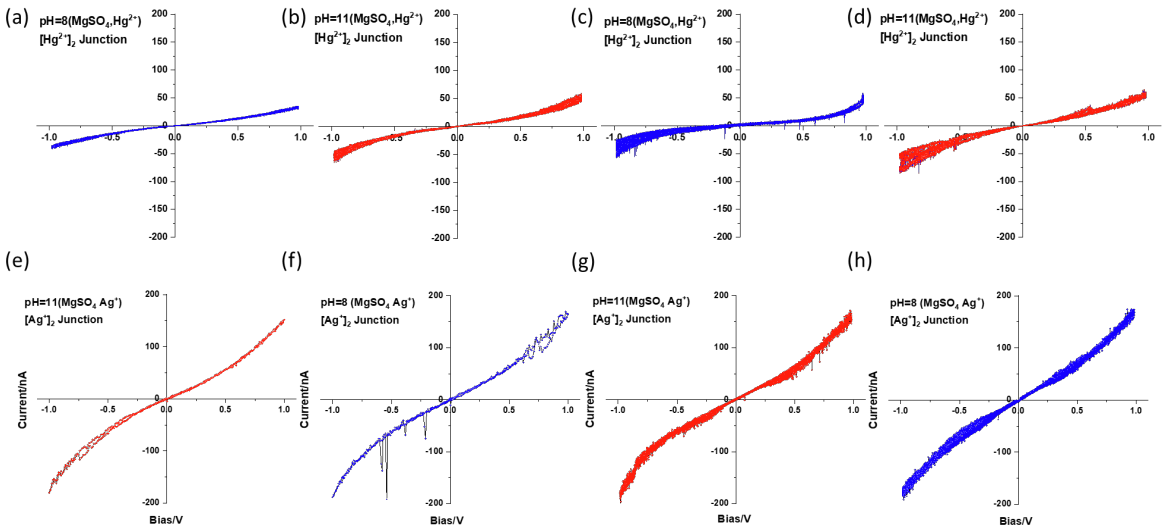


Figure S8. pH control with single ions (either Hg^{2+} or Ag^{+}) in solution. (a-d) *I-V* curves of $[Hg^{2+}]_2$ mCNT-DNA-mCNT junctions at different pHs with only Hg^{2+} present in the buffer. **(e-h)** *I-V* curves of $[Ag^{+}]_2$ mCNT-DNA-mCNT junctions at different pH with only Ag^{+} present in the buffers. Following the pH exchange order established in the mmDNA conductance switch experiment, we observed no significant alterations in the I-V characteristics of either $[Hg^{2+}]_2$ or $[Ag^{+}]_2$ junctions when exposed to their respective single-ion buffers. In conjunction with Figure 3, these findings strongly suggest that the synergistic interaction of multiple metallic ions is indispensable for the observed pH-dependent switching behavior.

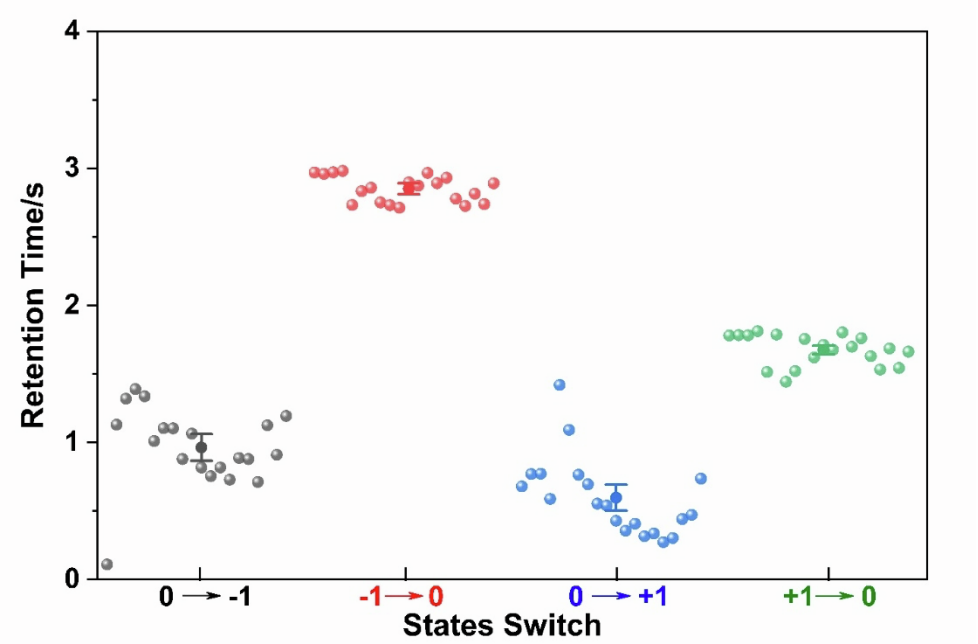
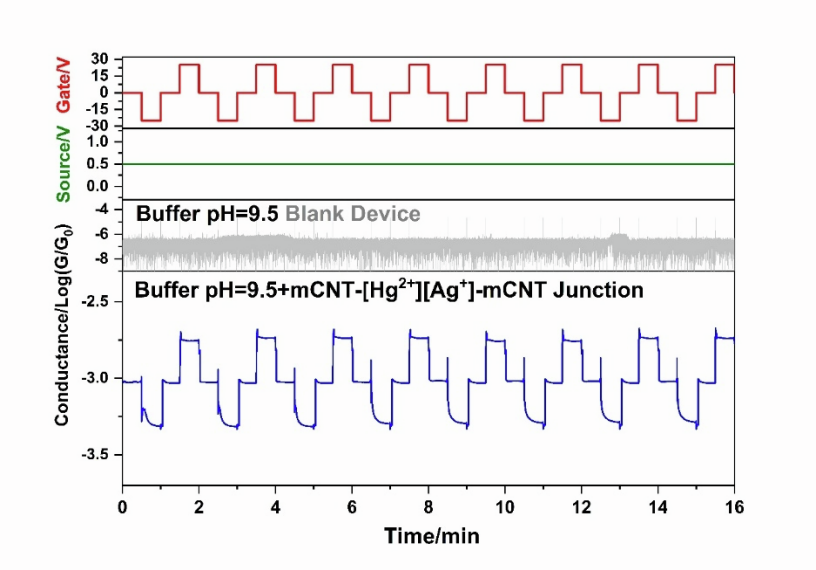


Figure S9. Statistical conductance retention plot for the mCNT-mmDNA-mCNT junctions, showing the average duration of state retention for each programmed state (+1, 0, -1) for each gate change (between +/-25 and 0 V). The error bars represent standard deviation, underscoring the variability in ion re-equilibration kinetics, supporting the device's potential as a volatile memory.

(a)



(b)

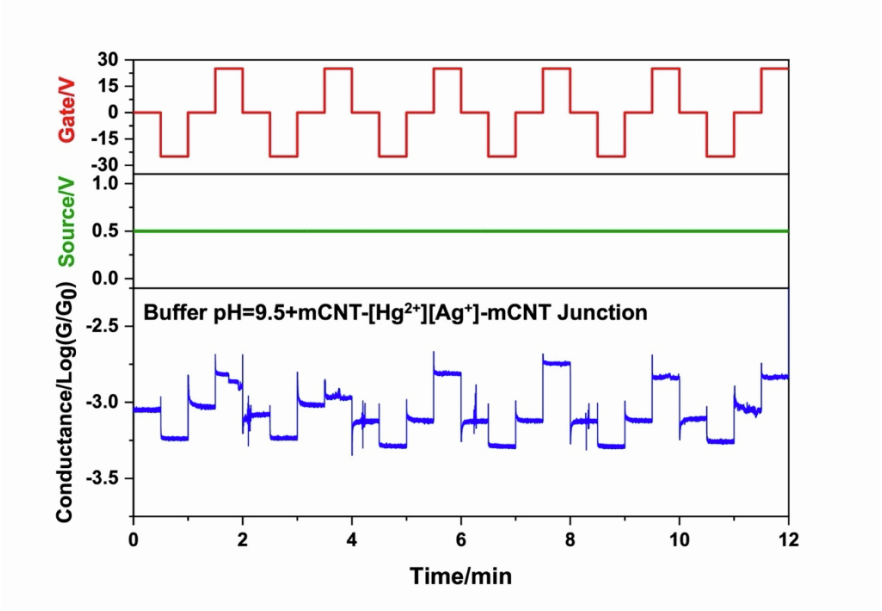


Figure S10. Reproducible gate-controlled switching of a mmDNA junction demonstrates its potential as a rewritable memory device. (a) Gate switching of a single mCNT-mmDNA-mCNT junction. The device was utilized as a rewritable memory device. By applying a square wave signal to the backgate electrode, we successfully modulated the mmDNA's states between [0], [-1], and [+1]. A source voltage of 0.5V allowed for the clear discrimination of conductance differences associated with these states. Gray curve represents a blank junction in buffer. **(b)** Conductance vs. time (bottom) plots for another representative mCNT-mmDNA-mCNT device undergoing the same gate-switching protocol as in (a). The conductance values remain consistent with those in (a), confirming reproducible state transitions across devices. Notable spikes during gate cycle changes may be caused by transient capacitive effects, such as double-layer charging or momentary ion redistribution at the junction interface.